JCB

Article

Rab18 promotes lipid droplet (LD) growth by tethering the ER to LDs through SNARE and NRZ interactions

Dijin Xu,[1]* Yuqi Li,[1]* Lizhen Wu,[1]* Ying Li,[1] Dongyu Zhao,[1] Jinhai Yu,[1] Tuozhi Huang,[1] Charles Ferguson,[2] Robert G. Parton,[2,3] Hongyuan Yang,[4] and Peng Li[1]

[1]State Key Laboratory of Membrane Biology, Tsinghua-Peking Center for Life Sciences, Beijing Advanced Innovation Center for Structural Biology, School of Life Sciences, Tsinghua University, Beijing, China
[2]Institute for Molecular Bioscience and [3]Centre for Microscopy and Microanalysis, University of Queensland, Brisbane, Australia
[4]School of Biotechnology and Biomolecular Sciences, University of New South Wales, Sydney, Australia

Lipid incorporation from endoplasmic reticulum (ER) to lipid droplet (LD) is important in controlling LD growth and intracellular lipid homeostasis. However, the molecular link mediating ER and LD cross talk remains elusive. Here, we identified Rab18 as an important Rab guanosine triphosphatase in controlling LD growth and maturation. *Rab18* deficiency resulted in a drastically reduced number of mature LDs and decreased lipid storage, and was accompanied by increased ER stress. Rab3GAP1/2, the GEF of Rab18, promoted LD growth by activating and targeting Rab18 to LDs. LD-associated Rab18 bound specifically to the ER-associated NAG-RINT1-ZW10 (NRZ) tethering complex and their associated SNAREs (Syntaxin18, Use1, BNIP1), resulting in the recruitment of ER to LD and the formation of direct ER–LD contact. Cells with defects in the NRZ/SNARE complex function showed reduced LD growth and lipid storage. Overall, our data reveal that the Rab18-NRZ-SNARE complex is critical protein machinery for tethering ER–LD and establishing ER–LD contact to promote LD growth.

Introduction

Lipid droplets (LDs), highly dynamic subcellular organelles primarily responsible for energy storage, have been linked to multiple cellular processes, including virus packing, protein storage and modification, and host defense (Herker et al., 2010; Klemm et al., 2011; Anand et al., 2012; Li et al., 2012; Suzuki et al., 2012). LDs contain a monolayer of phospholipids and their specific associated proteins, and undergo dynamic changes including biogenesis, fusion/growth, and degradation (Martin and Parton, 2006; Farese and Walther, 2009; Walther and Farese, 2012; Yang et al., 2012; Thiam et al., 2013; Pol et al., 2014). The dynamics of LDs reflect the lipid metabolic status, and uncontrolled growth of LDs has been linked to the development of multiple diseases including obesity, diabetes, fatty liver diseases, cardiovascular diseases, cancer, and neurodegenerative diseases (Gong et al., 2009; Greenberg et al., 2011; Suzuki et al., 2011; Xu et al., 2012a; Krahmer et al., 2013; Gross and Silver, 2014; Liu et al., 2015).

LD biogenesis is initiated and nascent LDs are formed from ER (Murphy and Vance, 1999; Khandelia et al., 2010; Zanghellini et al., 2010; Gross et al., 2011; Pol et al., 2014; Wilfling et al., 2014; Choudhary et al., 2015). The sizes of nascent LDs in mammalian cells are believed to be <100 nm, whereas most mature cytosolic LDs have diameters ranging from 0.25 to 100 µm depending on cell types (Pol et al., 2014). Several distinct mechanisms by which LDs grow and expand have been discovered. First, nascent LDs may grow to mature ones by acquiring neutral lipids from ER through continuous association with ER (Ohsaki et al., 2008; Jacquier et al., 2011), or by incorporation of ER-synthesized lipids that is dependent on DGAT1 activity through an unknown mechanism (Szymanski et al., 2007; Gross et al., 2011; Cartwright and Goodman, 2012; Xu et al., 2012b; Wilfling et al., 2013). Seipin, a protein originally identified in human general lipodystrophy (Magré et al., 2001; Payne et al., 2008), has shown to play an important role in promoting LD growth (Szymanski et al., 2007; Fei et al., 2008, 2011; Pagac et al., 2016; Salo et al., 2016; Wang et al., 2016) by localizing on a potential ER–LD contact site (Szymanski et al., 2007; Binns et al., 2010; Grippa et al., 2015; Han et al., 2015; Salo et al., 2016; Wang et al., 2016). Second, LD-associated enzymes such as GPAT4 and DGAT2 can promote LD growth by incorporating locally synthesized TAG into LDs (Fujimoto et al., 2007; Kuerschner et al., 2008; Krahmer et al., 2011; Wilfling et al., 2013). Finally, CIDE protein can promote LD growth via atypical lipid transfer and LD fusion in the white adipose tissue, in the liver of high-fat diet treated or obese mice, and in skin sebocytes and lactating mammary epithelia cells (Gong et al., 2011; Wang et al., 2012; Zhou et al., 2012; Wu et al., 2014b; Zhang et al., 2014; Xu et al., 2016).

*D. Xu, Y. Li, and L. Wu contributed equally to this paper.

Correspondence to Peng Li: li-peng@mail.tsinghua.edu.cn

The Rockefeller University Press
J. Cell Biol. Vol. 217 No. 3 975–995
https://doi.org/10.1083/jcb.201704184

Several factors including Perilipin, Rab8a, As160, and Mss4 that modulate Cidec-mediated LD fusion have been identified (Sun et al., 2013a; Wu et al., 2014a).

The activity of RabGTPases, crucial regulators of vesicle trafficking and membrane dynamics, is regulated by their specific GEFs, GAPs, and downstream effectors (Zerial and McBride, 2001; Grosshans et al., 2006; Stenmark, 2009). Rab18 is shown to be an LD-associated protein in several cell types including 3T3-L1 preadipocytes and differentiated adipocytes, and its expression levels and LD localization are controlled by specific nutritional or hormonal signals (Martin et al., 2005; Ozeki et al., 2005; Martin and Parton, 2008; Salloum et al., 2013). Rab18 has been shown to play a potential role in β-adrenergic–stimulated lipolysis and in insulin-induced lipogenesis in adipocytes (Pulido et al., 2011) and can facilitate hepatitis C virus replication by interacting with its nonstructural protein NS5A (Salloum et al., 2013). Interestingly, point mutations (L24Q or T95R, etc.) that results in defective Rab18 were discovered in autosomal recessive disorder Warburg Micro syndrome (WARBM; Bem et al., 2011). Mutations in *Rab3GAP1* (T18P and E24V) and *Rab3GAP2* (R426C; Handley and Aligianis, 2012) complex, a specific GEF for Rab18 (Gerondopoulos et al., 2014), were also identified in patients suffering from WARBM. Surprisingly, abnormal large LDs accumulate in fibroblasts isolated from WARBM patients who harbor Rab18 or Rab3GAP1/2 mutations (Aligianis et al., 2005; Handley and Aligianis, 2012; Handley et al., 2013; Liegel et al., 2013). A recent study showed that mammalian TRAPPII complex may act as a GEF of Rab18 to activate and recruit it to LDs in several cell types (Li et al., 2017). Despite all these analyses, the precise mechanism by which Rab18 controls LD dynamics remains unclear.

The yeast Dsl1 tethering complex is stably associated with three ER-associated Q-SNAREs (Ufe1p, Sec20p, and Use1p that have a glutamine at the center of their coiled-coil domain; Diefenbacher et al., 2011) and believed to play a central role in the tethering and fusion of Golgi-derived COPI transport vesicles to the ER (Andag et al., 2001; Kamena and Spang, 2004; Kraynack et al., 2005; Tagaya et al., 2014). Structural analysis revealed that the Dsl1 complex forms a 20-nm-tall "tower" from the ER surface (Ren et al., 2009; Tripathi et al., 2009). The NRZ tethering complex, the mammalian homologue of Dsl1 that includes ZW10 (Dsl1p), NAG (Dsl3p), and RINT1 (Tip20p), is associated with ER-localized Q-SNAREs (Use1, Syntaxin18, and BNIP1; Tagaya et al., 2014) and plays a potential role in Golgi-ER retrograde vesicle trafficking and fusion (Hatsuzawa et al., 2000; Burri et al., 2003; Hirose et al., 2004). Interestingly, a systemic screening of Rab effectors in *Drosophila melanogaster* cells reveals that the ZW10 and RINT1 subunits of the NRZ complex and Syntaxin18 of the ER–SNARE complex may be effectors of Rab18, and overexpression of Rab18 enhances the LD association of ZW10 (Gillingham et al., 2014).

Here, we have identified Rab18 as an important regulator of LD dynamics as its deficiency results in a defective LD growth and maturation without affecting LD biogenesis. Rab3GAP1/2 complex, the GEF of Rab18, promotes LD growth by activating and targeting Rab18 to LDs. Activated Rab18 binds to NRZ and ER-associated Q-SNAREs and recruits them to the close proximity of LDs. The Rab18-NRZ-SNARE interaction and complex formation result in tethering ER to LD and generating a close contact between the ER and LDs, therefore facilitating lipid incorporation to promote LD growth.

Results

Defective LD growth and maturation in *Rab18*-deficient cells

To identify RabGTPases that control LD dynamics, we knocked down 20 RabGTPases that were reported to be potentially localized to LDs in 3T3-L1 preadipocytes using their specific siRNAs (Wu et al., 2014a; Fig. 1 A). As control wild type or Rab10 knocking down cells accumulated a large number of LDs, knocking down Rab18 in 3T3-L1 preadipocytes led to the accumulation of fewer but significantly larger LDs (Fig. 1 B and Fig. S1 A). Knockout (KO) of Rab18 by CRISPR/Cas9 in 3T3-L1 preadipocytes also resulted in the accumulation of significantly fewer but larger LDs (Fig. 1 C and Fig. S1 B). When Rab18 was reintroduced into *Rab18*-deficient cells, LD size was reduced and the number of visible LDs was increased, showing a restoration of normal LD morphology (Fig. 1 C and Fig. S1 B).

To quantitatively evaluate the role of Rab18 in controlling LD dynamics, we systematically measured the number and sizes of LDs and the total volume of lipids in *Rab18*-deficient cells using a confocal optical section in combination with 3D surface reconstitution (Materials and methods). In control cells, ∼99% of LDs had a diameter ranging from 0.25 µm (limits of the fluorescent microscope) to 2 µm when cells were treated with oleic acid (OA; Fig. 1 D). LDs larger than 2 µm in diameter were rarely observed. As nascent LDs generated from ER were shown to have a size ranging from 60–100 nm in diameter, these droplets had to subsequently grow and mature via continuous TAG incorporation (Zanghellini et al., 2010; Pol et al., 2014; Wilfling et al., 2014; Fig. 1 E). We therefore define LDs ranging from 0.25 to 2 µm in diameter as mature LDs, and define LDs larger than 2 µm in diameter as supersized LDs.

In *Rab18*-deficient cells, the number of mature LDs in each cell was dramatically decreased (117 ± 13 per cell) compared with that in control cells (938 ± 105 per cell), representing an 88% reduction in the number of mature LDs (Fig. 1, D and F). The number and percentage of supersized LDs in each cell were significantly increased in *Rab18*-deficient cells (Fig. 1, D and G). When the sizes of the largest LD in a cell were measured in wild-type or *Rab18*-deficient cells, the mean diameter of the largest LD in *Rab18*-deficient cells was nearly twofold larger than that in control cells, representing an eightfold increase in LD volume (Fig. 1 H). Quantitative analysis also confirmed that reintroduction of Rab18 into *Rab18*-deficient cells increased the number of mature LDs but decreased the number of supersized LDs (Fig. 1 H).

To monitor the dynamic LD growth process under OA treatment, cells were first cultured in serum-free medium overnight to deplete existing LDs and then fed with OA. The morphology of LDs was continuously recorded under a time-lapse microscope. In control cells, a large amount of small LDs accumulated in the presence of OA. In *Rab18*-deficient cells, only a few LDs were observed, and these LDs expanded rapidly and grew into supersized ones (Fig. S1 C and Videos 1, 2, 3, and 4). Quantitative analysis of the dynamic LD growth process indicated that the rate of increase in the number and the total volume of mature LDs in *Rab18*-depleted cells were significant lower than in control cells (Fig. S1, D and E). However, the expansion of supersized LDs in *Rab18*-deficient cells was markedly faster (Fig. S1 F). The reduction of mature LD numbers and the appearance of supersized LDs were not a result of the fusion/coalescence of small LDs as this was not observed during the

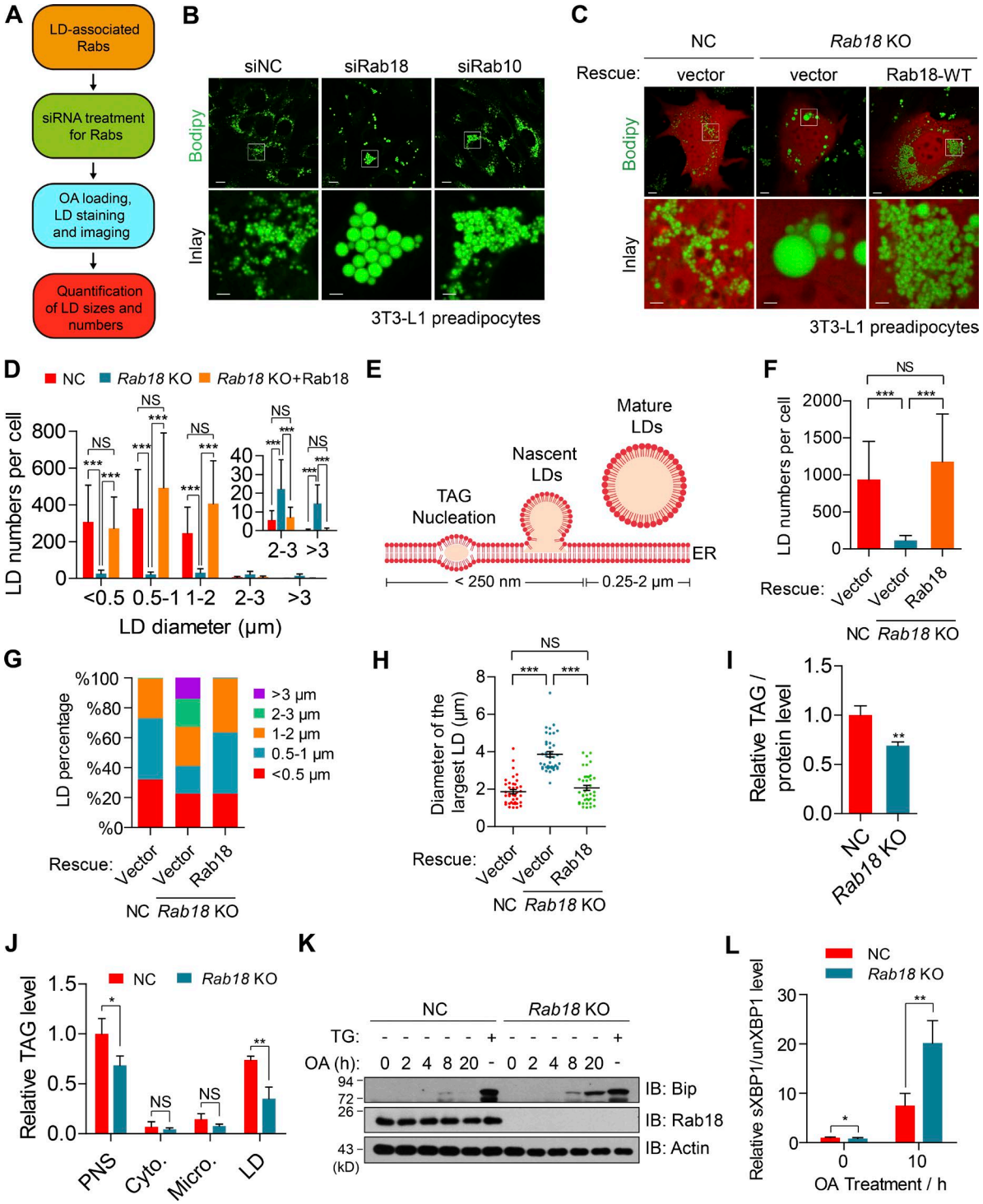

Figure 1. **Defective LD growth and maturation in *Rab18*-deficient cells. (A)** Outline of strategy to screen for LD-associated Rabs involved in LD growth. **(B)** Knocking down Rab18 alters LD morphology in 3T3-L1 preadipocytes. Bars: 10 μm; (insets) 2 μm. **(C)** Representative images of LDs (green) in negative control (NC) or *Rab18*-deficient (*Rab18* KO) 3T3-L1 preadipocytes. Red represents Cherry expression. Bars: 10 μm; (insets) 2 μm. **(D)** Histogram showing the mean number of LDs in each diameter in C. Data represent mean ± SD (n = 24 cells for NC; n = 25 cells for *Rab18* KO; n = 29 cells for *Rab18* KO+Rab18; ***, P < 0.001; NS, no significance by Kruskal-Wallis test). **(E)** Schematic diagram showing the process of LD biogenesis and growth. **(F–H)** Quantification of the number of mature LDs under fluorescent microscope (F), the percentage of LDs in each diameter (G), and diameter of the largest LD in each cell (H) in C. Mean ± SD for F, mean value for G, mean ± SEM for H, n = 24 cells for NC; n = 25 cells for *Rab18* KO; n = 29 cells for *Rab18* KO+Rab18; ***, P < 0.001; NS, no significance by Kruskal-Wallis test. **(I)** Reduced total TAG levels in *Rab18* KO 3T3-L1 preadipocytes. TAG/protein level of control cells was normalized to 1. Three independent experiments were performed. Mean ± SD; n = 3; **, P < 0.01 by two-tailed t test. **(J)** Relative TAG level in various subcellular fractions. TAG level in PNS in control cells was normalized to 1. Three independent experiments were performed. Mean ± SD; n = 3; *, P < 0.05; **, P < 0.01; NS, no significance by two-tailed t test. **(K and L)** Increased BIP expression and mRNA levels of spliced XBP-1 in *Rab18* KO 3T3-L1 preadipocytes after OA (400 μM) treatment. Cells treated with 1 μM TG for 6 h were used as a positive control. Three independent experiments were performed. Mean ± SD; n = 3; *, P < 0.05; **, P < 0.01 by two-tailed t test. All experiments were performed at least twice. WT, wild type.

live-cell imaging recording process (Video 2). Overall, these data strongly suggest that depletion of Rab18 disrupted normal LD morphology, leading to a significant reduction in the number of mature LDs but accumulation of a few supersized LDs.

Next, we measured the amount of total cellular TAG and its subcellular distribution in *Rab18*-deficient cells and observed significantly lower cellular TAG and reduced TAG levels in the LD fraction in *Rab18*-deficient cells after they were treated with OA for 20 h (Fig. 1, I and J). Similar rates of fatty acid (FA) uptake and TAG hydrolysis were observed between wild-type and *Rab18*-deficient cells (Fig. S1, G and H). However, *Rab18*-deficient cells had a decreased TAG synthesis (Fig. S1, I and J). As long-term exposure to excess FA results in a chronic ER stress in cells lacking the capacity to synthesize or store neutral lipids (Ota et al., 2008; Chitraju et al., 2017), we evaluated the role of Rab18 in FA overloading–induced ER stress. As shown in Fig. 1 K, expression levels of Bip, a specific ER stress marker, were significantly increased in the presence of thapsigargin (TG), a known reagent to induce ER stress. The expression levels of Bip were also increased in *Rab18*-deficient cells with a prolonged OA treatment. Splicing levels of XBP-1, another ER stress marker, was also significantly increased in *Rab18*-deficient cells (Fig. 1 L). Therefore, Rab18 plays an important role in regulating lipid storage, and its deficiency results in reduced lipid storage and increased ER stress in the presence of excess free FAs.

Rab18 deficiency causes abnormal LD growth in adipocytes and Leydig cells

As Rab18 was previously shown to be highly expressed in differentiated adipocytes, we knocked down Rab18 in 3T3-L1 adipocytes and observed that these cells contained larger LDs compared with those in control adipocytes (Fig. 2, A and B). In contrast, overexpression of Rab18 in adipocytes resulted in a dramatic decrease in LD sizes (Fig. 2, C and D). In addition, depletion of Rab18 in adipocytes led to a 20% reduction in the cellular TAG levels (Fig. 2 E) and an ∼15% decrease in basal and stimulated lipolysis (Fig. 2 F). This minor decrease in lipolysis is probably a result of a secondary effect of increased LD sizes and decreased LD surface area in *Rab18*-depleted adipocytes. Rab18 expression is also observed in Leydig cells that contain large amounts of LDs and are responsible for the production of testosterone in testes (Yamaguchi et al., 2015; Shen et al., 2016). We generated *Rab18*-deficient TM-3 (a Leydig cell line) cells and observed that *Rab18*-deficient TM-3 cells contained less mature LDs but an increased number of supersized LDs after OA treatment (Fig. 2, G and H). Overall, these data indicate that Rab18 regulates the LD morphology and lipid storage in adipocytes and Leydig cells.

Rab18 controls the growth of nascent LDs

As *Rab18* depletion dramatically reduced the number of mature LDs, we checked whether its deficiency would disrupt LD biogenesis and nascent LD formation by expressing GFP-*LiveDrop*, a nascent LD marker (Wang et al., 2016), in *Rab18*-deficient cells or in control wild-type cells. Cells were starved for 16 h to deplete the existing LDs. After short-term OA treatment (1 h), similar numbers of *LiveDrop*-positive LDs, representing nascent LDs, accumulated in both *Rab18*-deficient and control cells (Fig. 3, A and B). In control cells, *LiveDrop*-positive signals overlapped very well with LipidTOX (65.6%) signals that stain mature LDs. However, in *Rab18*-deficient cells, only a small percentage of *LiveDrop* positive signals (8.09%) overlapped with LipidTOX-positive mature LDs (Fig. 3 C). After cells were treated with OA for 4 h, a majority of *LiveDrop*-positive LDs were also positive for LipidTOX signals in control cells. On the contrary, in *Rab18*-deficient cells, most *LiveDrop*-labeled LDs remained small and did not overlap with LipidTOX staining (Fig. 3 D). Therefore, Rab18 does not appear to affect LD biogenesis but is responsible for the growth and maturation of nascent LDs.

To further confirm the role of Rab18 in regulating the growth of nascent LDs, we examined LD morphology of *Rab18*-deficient cells by EM analysis. The presence of nascent LDs within the sizes of 100–200 nm in diameter was observed in both control and *Rab18*-deficient cells 1 h after OA treatment (Fig. 3 E). Quantitative analysis indicated that the number of nascent LDs was slightly increased in *Rab18*-deficient cells compared with that in control cells (Fig. 3 F). After 8 h of OA treatment, the total number of LDs visible in EM analysis showed no significant difference between control and *Rab18*-deficient cells. However, LD size distribution changed dramatically (Fig. 3, E, G, and H). In wild-type cells, the majority of nascent LDs had grown larger than 150 nm in diameter. In contrast, LDs with diameter larger than 150 nm (except a few LDs larger than 2 µm in diameter) were rarely observed in *Rab18*-deficient cells. Instead, the majority of LDs remained smaller than 150 nm in *Rab18*-deficient cells (Fig. 3, E, G, and H). In summary, EM analysis confirmed that *Rab18* deficiency did not affect LD biogenesis and nascent LD formation but controlled the growth of nascent LDs into mature LDs.

Rab18-mediated LD growth and maturation are dependent on lipid synthesis in ER

To evaluate the role of TAG synthesis enzymes in Rab18-mediated LD growth, we checked the expression levels and subcellular distribution of DGAT1/2 and GPAT3/4 in *Rab18*-deficient cells and found that Rab18 deficiency affected neither their expression (Fig. S2 A) nor their subcellular distribution (Fig. S2, B–G). Inhibition of DGAT1 activity led to the accumulation of a significantly lower number of mature LDs and decreased cellular TAG (Fig. 4, A and B; Wilfling et al., 2013) in wild-type cells and reduced LD sizes in *Rab18*-deficient cells. On the contrary, overexpression of DGAT1 in wild-type cells increased the number of mature LDs by about twofold (Fig. 4, C and D). However, overexpression of DGAT1 in *Rab18*-deficient cells did not restore the number of mature LDs (Fig. 4, C and D). Surprisingly, inhibition of DGAT2 did not affect the number of mature LDs in wild-type cells as well as the sizes of LDs in *Rab18*-deficient cells (Fig. 4, E and F). Knocking down both GPAT3 and GPAT4, which act as rate-limiting enzymes in the TAG synthesis pathway upstream of DGAT1 and DGAT2, reduced the number of mature LDs and the intracellular TAG level in wild-type cells (Fig. 4, G and H) and decreased LD sizes in *Rab18*-deficient cells (Fig. 4, G and H). These data suggest that TAG synthesis on ER that is controlled by DGAT1/GPAT3/4 was responsible for the formation of supersized LDs, whereas local TAG synthesis mediated by DGAT2 did not contribute to the formation of supersized LDs in *Rab18*-deficient cells. Consistent with Chitraju et al. (2017), we observed increased FA overloading–induced ER stress in wild-type cells when DGAT1 was inhibited (Fig. 4 I). In *Rab18*-deficient cells, ER stress was induced under the FA overloading condition and further enhanced when DGAT1 (but not DGAT2) was inhibited (Fig. 4 I). Overall, we demonstrated that Rab18-mediated LD growth and maturation are dependent on TAG synthesis on ER,

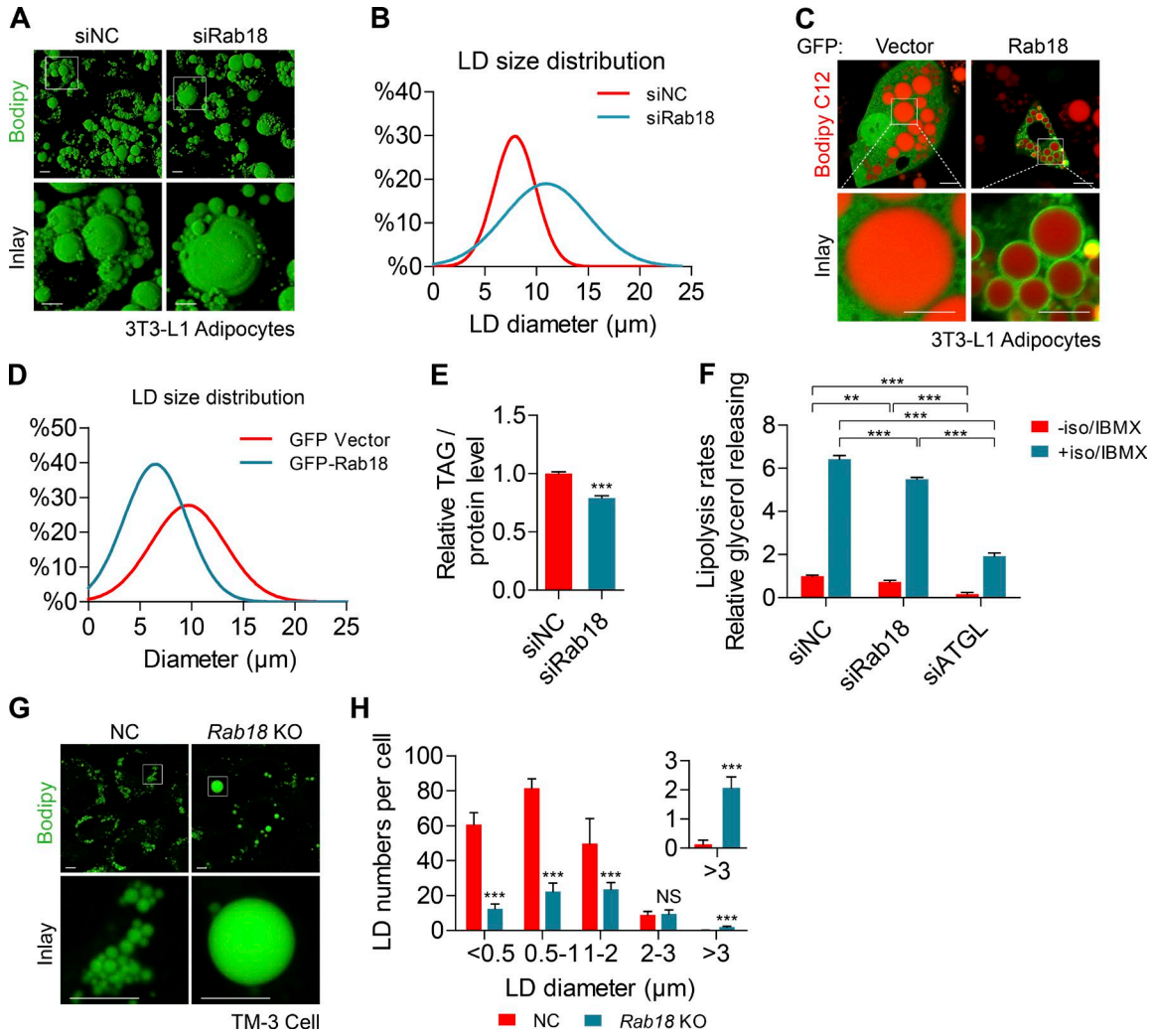

Figure 2. **Rab18 deficiency causes abnormal LD growth in adipocytes and Leydig cells. (A and B)** Knocking down Rab18 alters LD (green) sizes in adipocytes. Bars: 10 μm; (insets) 5 μm. (B) Size distribution of the largest LD. LDs from 88 siRab18-transfected cells and 116 siNC-transfected cells were analyzed (pooled from three experiments). LD size distribution was fitted with Gaussian function. **(C and D)** Overexpressing Rab18 decreases LD sizes in adipocytes. Green, GFP; red, LDs. Bars: 10 μm; (insets) 5 μm. (D) The size distribution of the largest LD. LDs from 121 Rab18-transfected cells and 100 vector-transfected cells were analyzed (pooled from three experiments). LD size distribution was fitted with Gaussian function. **(E)** Relative cellular TAG levels in adipocytes. TAG/protein level of siNC was normalized to 1. Three independent experiments were performed. Mean ± SD; $n = 3$; ***, $P < 0.001$ by two-tailed *t* test. **(F)** Reduced basal and stimulated lipolysis in *Rab18* knockdown adipocytes. The amount of free glycerol released from siNC cells without the treatment of isoproterenol (iso) and 3-isobutyl-1-methylxanthine (IBMX) was normalized to 1. Three independent experiments were performed. Mean ± SD; $n = 3$; **, $P < 0.01$; ***, $P < 0.001$ by one-way ANOVA with Tukey post hoc tests. **(G and H)** *Rab18* deficiency in TM-3 Leydig cell alters LD morphology. Green, LDs. Bars: 5 μm; (insets) 2 μm. (H) Histogram showing the mean number of LDs in G. Mean ± SD; $n = 10$; ***, $P < 0.001$; NS, no significance by two-tailed *t* test. All experiments were performed at least twice.

and Rab18 may play a role in mediating the transfer of ER-synthesized lipids to nascent LDs.

Rab3GAP1/2 controls the activity and LD localization of Rab18

To delineate the mechanism by which Rab18 controls LD growth, we checked its subcellular localization and observed that endogenous Rab18 was associated with LDs in 3T3-L1 preadipocytes (Fig. 5 A). Biochemical fractionation further confirmed that Rab18 was highly enriched in the LD fraction (Fig. 5 B). In serum-free medium, Rab18 was observed at specific loci on ER and associated with nascent LDs when cells were treated with FAs, overlapping with ACSL3, an early LD marker (Kassan et al., 2013; Fig. 5 C). Rab3GAP1/2 complex, a GEF of Rab18, was also localized to LD when Rab3GAP2 was coexpressed with Rab18 in 3T3-L1 preadipocytes (Fig. 5 D). Colocalization of Rab3GAP1, Rab3GAP2, and Rab18 was also observed at the newly synthesized LDs (Fig. S3 A). When Rab18 was introduced into *Rab3GAP1*- or *Rab3GAP2*-deficient cells, the LD localization of Rab18 was completely abolished in these cells (Fig. 5 E and Fig. S3 B). Biochemical fractionation also showed that the enrichment of Rab18 on LD fraction was abolished in cells deficient in *Rab3GAP1* (Fig. 5 F).

We then checked the LD morphology in *Rab3GAP1*- or *Rab3GAP2*-deficient 3T3-L1 preadipocytes (Fig. 5 G; and Fig. S3, B and C) and observed that the number and percentages of mature LDs in these cells were dramatically reduced (41 ± 2 per cell in *GAP1* KO cells or 33 ± 1 per cell in *GAP2* KO cells vs. 612 ± 28 per cell in wild-type cells, representing a nearly 95% reduction; Fig. 5, G and H; and Fig. S3, C and D). Instead, both *Rab3GAP1*- and *Rab3GAP2*-deficient cells accumulated supersized LDs (Fig. 5, G and H; and Fig. S3, C, E, and F),

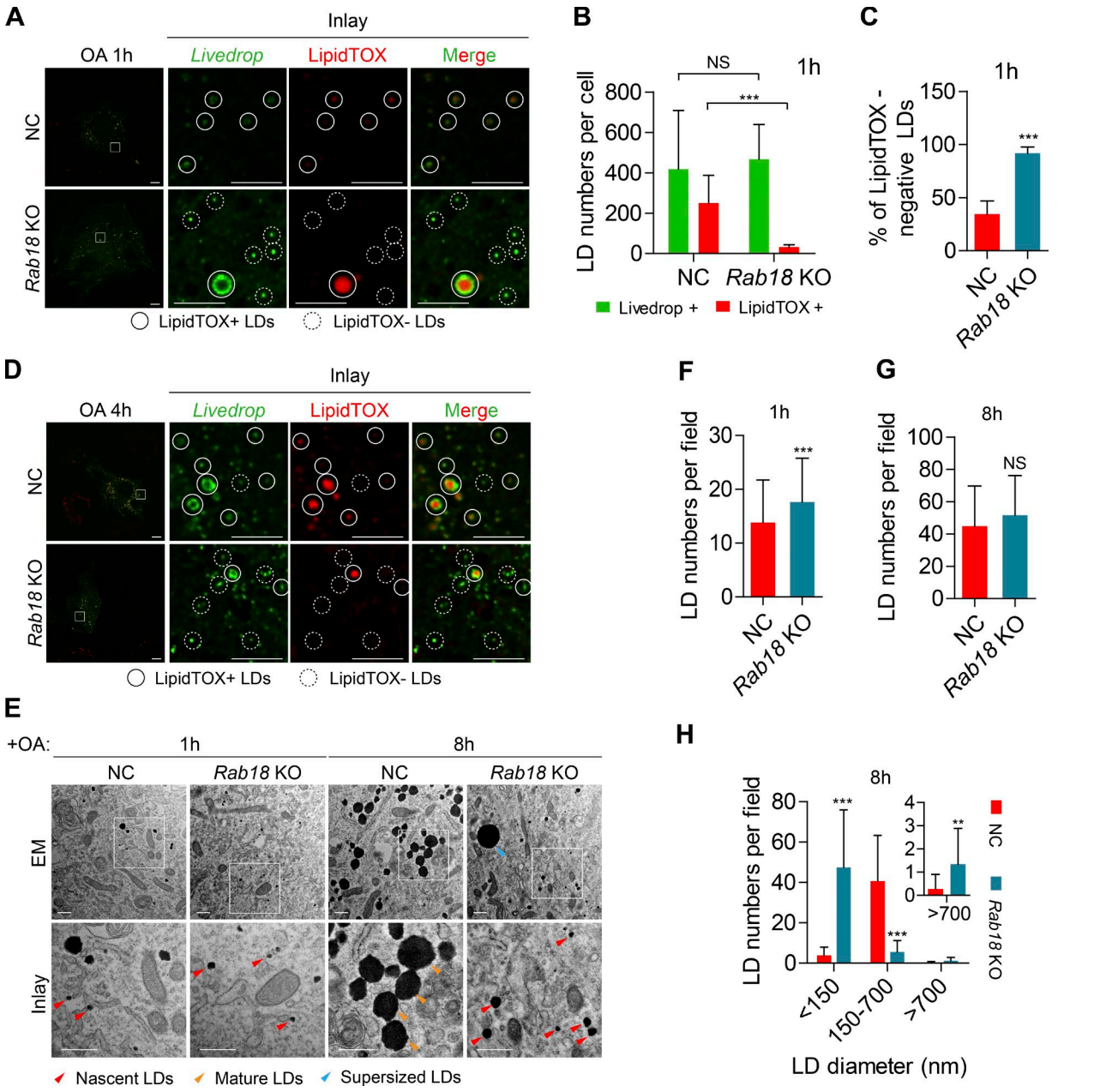

Figure 3. **Rab18 controls the growth of nascent LDs. (A–C)** Similar number of nascent LDs labeled with GFP-*LiveDrop* in control and *Rab18* KO cells. Green, GFP-*LiveDrop*; red, LipidTOX neutral red. Circles, LipidTOX-positive LDs; dotted line circles, LipidTOX-negative LDs. Bars: 5 µm; (insets) 2 µm. (B) Quantification of the number of *LiveDrop*-positive LDs and LipidTOX-positive LDs. Mean ± SD; $n = 10$ for control cells, $n = 11$ for *Rab18* KO cells; NS, no significance; ***, $P < 0.001$ by two-tailed *t* test. (C) The percentage of LDs that were *LiveDrop*-positive but LipidTOX-negative. Mean ± SD; $n = 10$ for control cells, $n = 11$ for *Rab18* KO cells; ***, $P < 0.001$ by Mann-Whitney test. **(D)** Representative images showing *LiveDrop*-positive (green) LDs in cells treated with OA for 4 h. Red, LipidTOX neutral red. Bars: 5 µm; (insets) 2 µm. **(E)** Representative EM images showing the LD morphology in *Rab18* KO and in control 3T3-L1 preadipocytes. Red arrows, the nascent LDs; orange arrows, the mature LDs; blue arrows, the supersized LDs. Bars, 500 nm. **(F)** Number of LDs in randomly selected EM image fields in cells treated with OA for 1 h in E. Mean ± SD; $n = 147$ ROIs for control cells, $n = 154$ ROIs for *Rab18* KO cells; ***, $P < 0.001$ by Mann-Whitney test. **(G and H)** Total number of LDs (G) and the mean number of LDs in each diameter in cells (H) that were treated with OA for 8 h in E. Mean ± SD; $n = 22$ ROIs for control cells, $n = 29$ ROIs for *Rab18* KO cells; **, $P < 0.01$; ***, $P < 0.001$; NS, no significance by Mann-Whitney test. All experiments were performed at least twice.

similar to those in *Rab18*-deficient cells. Consistent with reduced mature LDs, the total amount of cellular TAG in these cells was also decreased (Fig. S3 G). In mature adipocytes, both Rab3GAP1 and Rab3GAP2 were markedly increased during the course of adipocyte differentiation (Fig. S3 H) and colocalized with Rab18 on LDs, consistent with the observation in preadipocytes (Fig. S3 I). *Rab3GAP1* deficiency in adipocytes did not affect 3T3-L1 differentiation as the expression levels of FABP4, Plin1, and Fsp27 were similar between wild-type and *Rab3GAP1*-deficient cells (Fig. S3 J). Similar to the observation in *Rab18*-deficient adipocytes, *Rab3GAP1*-deficient adipocytes accumulated fewer but larger LDs (Fig. 5 I and Fig. S3 K). Overall, these data strongly indicate that Rab3GAP1/2 acts as a GEF to promote the LD localization and activation

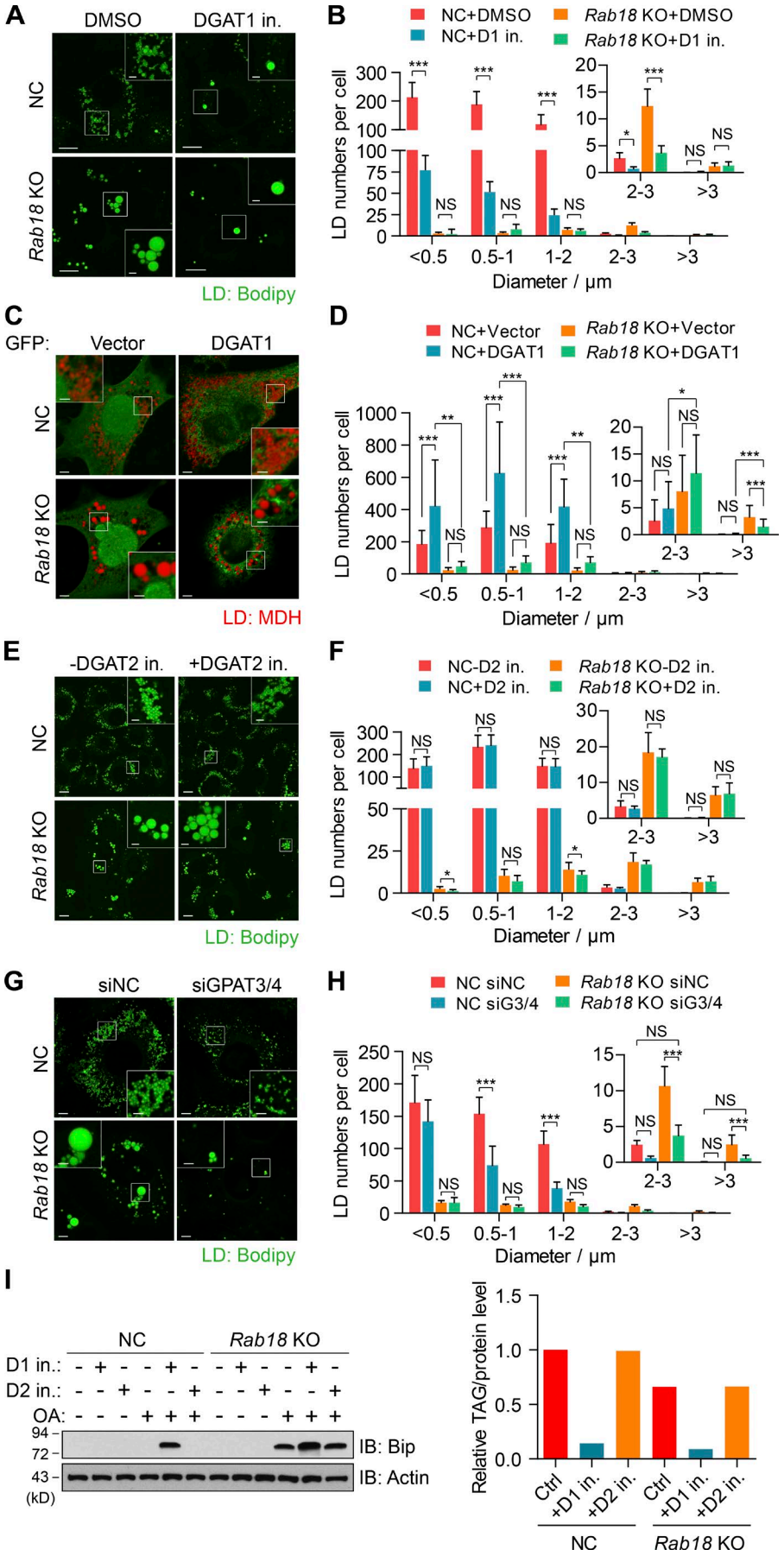

Figure 4. **TAG synthesis on ER is required for Rab18-controled LD growth. (A and B)** Inhibition of DGAT1 activity reduced the size and number of LDs in both control (NC) and *Rab18* KO cells. 1 μM of DGAT1 inhibitor (DGAT1 in.) was used. Green, LDs. Bars: 10 μm; (insets) 2 μm. Histogram in B showing the mean number of LDs in each diameter in A. Mean ± SD; n = 11–18 for each genotype; *, P < 0.05; ***, P < 0.001; NS, no significance by two-tailed t test. **(C and D)** *Rab18* KO cells expressing DGAT1 did not accumulate mature LDs. Red, LDs. Bars: 5 μm; (insets) 2 μm. Histogram in D showing the mean number of LDs in each diameter in C. Mean ± SD; n = 19–28 cells for each genotype; *, P < 0.05; **, P < 0.01; ***, P < 0.001; NS, no significance by two-tailed t test. **(E and F)** Inhibition of DGAT2 did not affect the numbers and sizes of LDs in *Rab18* KO cells. 2 μM of DGAT2 inhibitor was used. Bars: 10 μm; (insets) 2 μm. Histogram in F showing the mean number of LDs in each diameter in E. Mean ± SD; n = 9–11 for each genotype; *, P < 0.05; NS, no significance by two-tailed t test. **(G and H)** Knocking down GPAT3/4 reduced the number and sizes of mature LDs in *Rab18* KO cells. Bars: 5 μm; (insets) 2 μm. Histogram in H showing the mean number of LDs in each diameter in G. Mean ± SD; n = 10; *, P < 0.05; ***, P < 0.001; NS, no significance by two-tailed t test. **(I)** Reduced TAG and increased ER stress in *Rab18* KO cells treated with FAs. Left: Representative Western blot showing the ER stress in *Rab18* KO cells. From three independent experiments. Right: Subcellular TAG levels of one representative experiment. All experiments were performed at least twice.

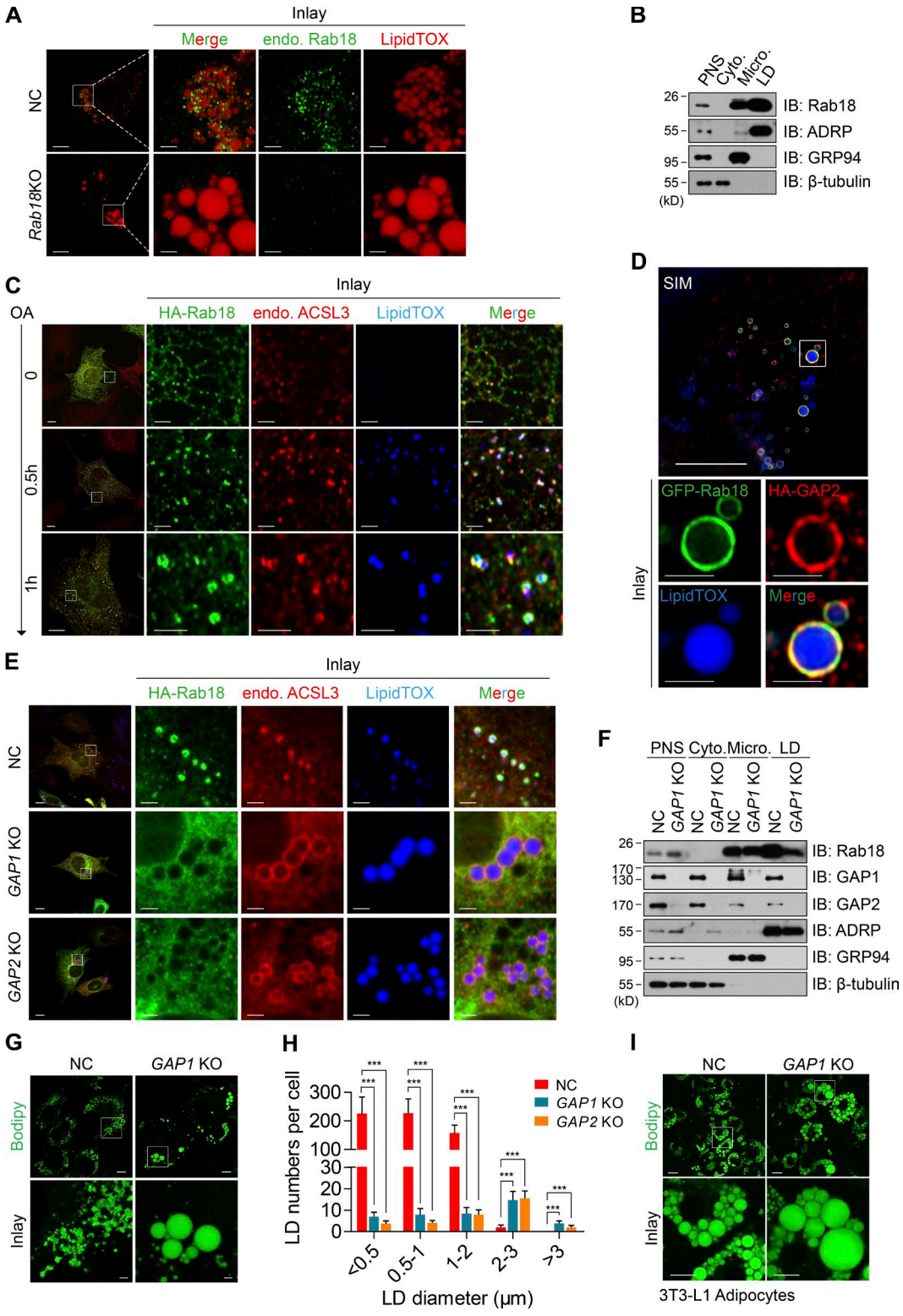

Figure 5. **Rab3GAP1/2 controls the activity and LD localization of Rab18. (A)** Endogenous Rab18 (green) was associated with LDs (red) in 3T3-L1 preadipocytes. Bars: 10 µm; (insets) 2 µm. **(B)** Rab18 was enriched in LD fraction isolated from 3T3-L1 preadipocytes. ADRP, LD marker; GRP94, a microsomal marker; β-tubulin, a cytosol marker. **(C)** Rab18 (green) was associated with LD (blue) at early stage of LD biogenesis. Red, endogenous ACSL3. Bars: 10 µm; (insets) 2 µm. **(D)** Representative SIM superresolution images showing the localization of HA-Rab3GAP2 (red) and GFP-Rab18 (green) on LDs (blue). Bars: 10 µm; (insets) 1 µm. **(E)** Rab18 (green) was not localized to LDs (blue) in *Rab3GAP1*- or *Rab3GAP2*-deficient cells. Red, ACSL3. Bars: 10 µm; (insets) 2 µm. **(F)** Rab18 was not enriched in the LD fraction in *Rab3GAP1*-deficient cells. **(G and H)** Reduced mature LDs and the presence of supersized LDs in *Rab3GAP1/2*-deficient cells. Bars: 10 µm; (insets) 2 µm. Histogram in H showing the mean number of LDs in each diameter in G. Mean ± SD; $n = 13$ for control cells, $n = 20$ for *Rab3GAP1* KO cells, $n = 16$ for *Rab3GAP2* KO cells; ***, $P < 0.001$ by one-way ANOVA with Tukey post hoc tests. **(I)** Increased LD (green) sizes in *Rab3GAP1*-deficient adipocytes. Bars: 10 µm; (insets) 5 µm. All experiments were performed at least twice.

of Rab18 in controlling LD growth and maturation in both pre- and mature adipocytes.

Rab18 binds to ZW10 and forms a complex with NRZ tethering proteins

Because NRZ tethering complex that comprises NAG, RINT1, and ZW10 has been reported to interact with Rab18 (Gillingham et al., 2014), we further confirmed their interaction by overexpressing FLAG-Rab18 and checked the presence of endogenous NRZ proteins in the Rab18–immunoprecipitation (IP) products. Endogenous NAG and ZW10 were detected in the precipitates (Fig. 6 A). The amount of coprecipitated NAG and ZW10 was increased in the presence of Rab3GAP1/2. RINT1, the third component in the NRZ complex, was also detected in the Rab18-IP product in the presence of Rab3GAP1/2 (Fig. 6 A). To test the interaction of Rab18 with individual subunits in the NRZ complex, we first coexpressed ZW10 and Rab18 in 293T cells, and observed that ZW10 and Rab18 were able to reciprocally pull down each other (Fig. 6, B and C). To ascertain the direct interaction between Rab18 and ZW10, we purified Flag-ZW10 from 293T cells and GST-Rab18 from *Escherichia coli* (Fig. S4 A) and performed in vitro binding assays. As shown in Fig. 6 D, GST-Rab18 was able to specifically pull down ZW10 in the presence of GTPγS that locked Rab18 in its GTP-bound form. We then generated serial truncations of ZW10 and identified that its C terminus was necessary for its interaction with Rab18 (Fig. S4, B and C). ZW10 truncation lacking the C-terminal region still bound to NAG and RINT1, consistent with previous observation (Arasaki et al., 2006) that the N-terminal region of ZW10 mediates its interaction with NAG/RINT1. NAG alone showed weak interaction with Rab18, and its association with Rab18 was dramatically increased in the presence of ZW10 (Fig. 6 E). Truncation analysis further revealed that the C-terminal region (aa 1355–2371) of NAG mediated its interaction with ZW10 and Rab18 (Fig. 6 E and Fig. S4 D). These data suggest that ZW10 in the NRZ complex interacts directly with the GTP-bound form of Rab18, and its C-terminal region is essential for this interaction.

To check whether Rab18 affects the subcellular distribution of NRZ complex, we first isolated various subcellular fractions from wild-type or *Rab18*-deficient TM-3 cells (Fig. 6 F). Components of NRZ complex including ZW10 and NAG were detected in both ER and LD fractions in wild-type cells. However, their presence in the LD fraction was completely abolished in the absence of Rab18. When Cherry-ZW10 and HA-Rab18 were coexpressed in 3T3-L1 preadipocytes, both endogenous NAG and Cherry-ZW10 were observed on the LD surface, colocalizing with Rab18 (Fig. 6 G). In addition, introduction of Rab18 into 3T3-L1 preadipocytes markedly enhanced the LD localization of endogenous NAG and ZW10 (Fig. 6 H). RINT1 was also observed on the LD surface (Fig. S4 E). When GFP-ZW10 was introduced into mature adipocytes, the LD association of ZW10 was observed only when it was coexpressed with wild-type Rab18 but not with Rab18-C203A (Fig. S4 F). These data indicate that Rab18, in its GTP-bound form, interacts with and recruits the NRZ complex to the LD surface.

NRZ tethering complex act as a downstream effector of Rab18 to control LD growth

To evaluate the function of the NRZ complex in regulating LD growth, we knocked out *NAG* or *ZW10* in 3T3-L1 preadipocytes (Fig. S5 A). Depletion of *NAG* or *ZW10* led to the accumulation of significantly fewer but larger LDs (Fig. 7 A). Quantitative analysis of LD morphology showed that *NAG* or *ZW10* deficiency resulted in a dramatic reduction in the number and percentage of mature LDs after OA treatment (218 ± 6 per cell in *NAG*-deficient cells or 297 ± 19 per cell in *ZW10*-deficient cells vs. 557 ± 22 per cell in wild-type cells, representing a nearly 50% reduction; Fig. 7, B and C; and Fig. S5 B). On the contrary, numbers of supersized LDs were significantly increased in *NAG*- or *ZW10*-deficient cells (Fig. 7 B and Fig. S5, B and C). Similar to the observation in *Rab18*-deficient cells, time-lapse imaging showed that *NAG*-deficient cells accumulated a few large LDs that expanded rapidly (Fig. S5, D–G; and Videos 5 and 6). In addition, levels of total cellular TAG were significantly decreased in *NAG*- or *ZW10*-deficient cells (Fig. 7 D), and the susceptibility of long-term FA–induced ER stress was increased in *NAG*-deficient cells (Fig. 7 E). In addition, overexpressing Rab18 in *NAG*-deficient cells did not increase the number of mature LDs (Fig. 7, F and G) or decrease the size of supersized LDs (Fig. 7, F and H). Importantly, when truncated ZW10 that is defective in interacting with Rab18 was introduced into *ZW10*-deficient cells (Fig. S5 H), it did not restore its function in promoting LD growth and maturation (Fig. S5, I and J). These data indicate that NRZ complex acts downstream of Rab18, and the interaction between Rab18 and NRZ is crucial for its role in promoting LD growth and maturation.

To test whether NAG controls LD biogenesis, we expressed GFP-*LiveDrop* in wild-type or *NAG*-deficient cells. 4 h after OA treatment, the majority of *LiveDrop*-positive LDs overlapped with LipidTOX in wild-type cells. In *NAG*-deficient cells, a large number of *LiveDrop*-positive LDs accumulated, and they did not overlap with the LipidTOX signal (Fig. S5 K). EM analysis showed that nascent LDs <150 nm in diameter were present in both wild-type and *NAG*-deficient cells 1 h after OA treatment (Fig. 7 I), and the number of nascent LDs was slightly increased in *NAG*-deficient cells (Fig. 7 J). After prolonged OA treatment (8 h), the total number of LDs visible in EM analysis showed no significant difference between wild-type and *NAG*-deficient cells (Fig. 7, I and K). However, in *NAG*-deficient cells, the majority of LDs had a diameter less than 150 nm, and a few supersized LDs were observed (Fig. 7, I and L). These data indicate that *NAG* deficiency does not affect LD biogenesis but controls the growth of nascent LDs to form mature LDs, almost completely recapitulating the phenotype of *Rab18* and *Rab3GAP1/2* deficiencies.

ER-associated SNAREs control Rab18-mediated LD growth

As the NRZ complex has been reported to interact with ER-associated Q-SNAREs including Syntaxin18, Use1, and BNIP1 (Hatsuzawa et al., 2000; Hirose et al., 2004; Nakajima et al., 2004), we tested whether these proteins play roles in regulating LD growth by knocking them out in 3T3-L1 preadipocytes (Fig. 8 A). A loss of any member of the Q-SNAREs resulted in a reduction of the accumulation of mature LDs (110 ± 3 per cell in *Stx18* KO cells, 166 ± 5 per cell in *Use1* KO cells, and 161 ± 7 per cell in *BNIP1* KO cells vs. 593 ± 24 per cell in wild-type cells, representing a nearly 75% reduction; Fig. 8, B–D), whereas the number of supersized LDs was significantly increased and levels of cellular TAG were markedly reduced in *Stx18*-, *Use1*-, or *BNIP1*-deficient cells after prolonged OA treatment (Fig. 8, B, E, and F). As three Q-SNAREs and one

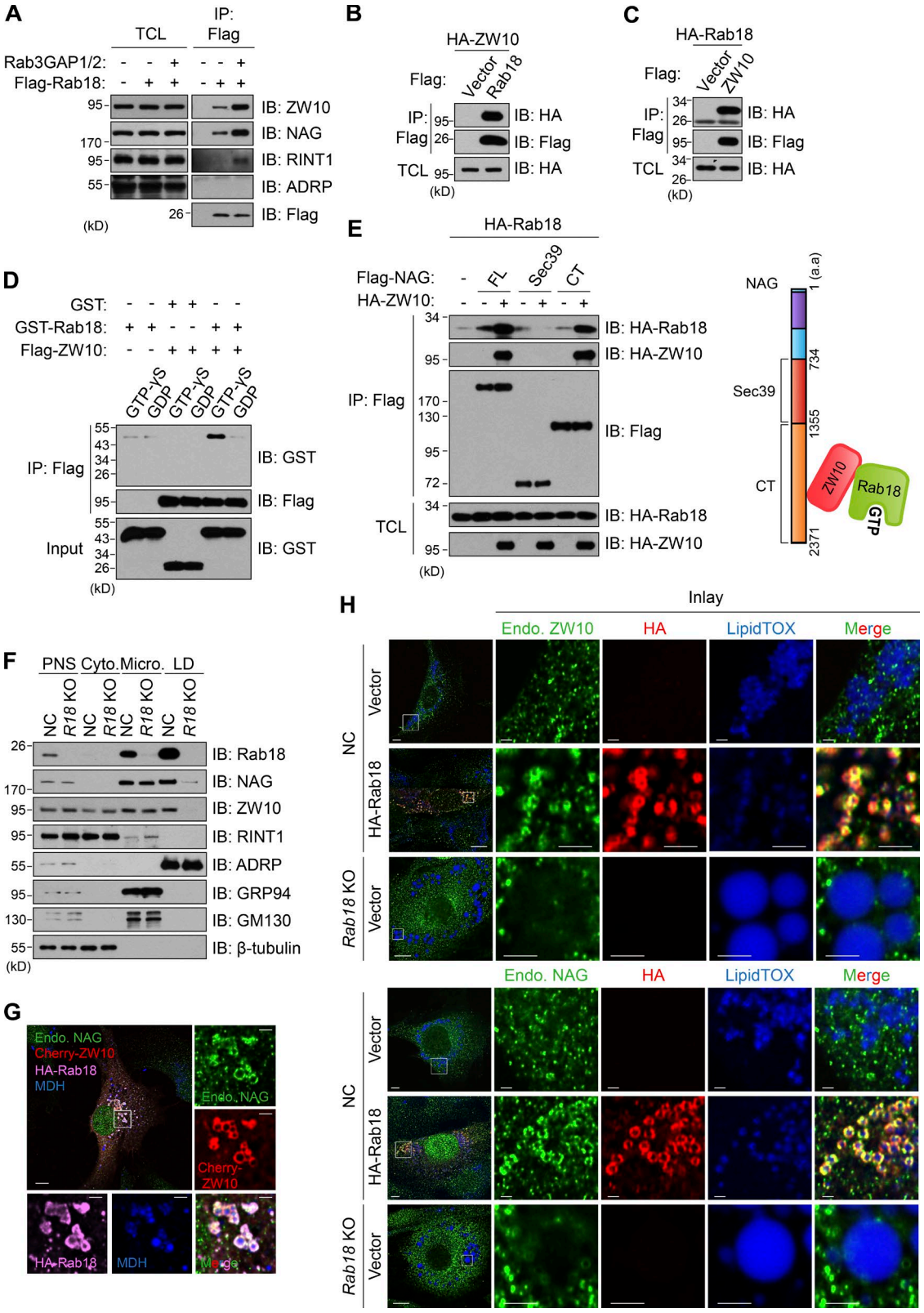

Figure 6. **Rab18 binds to NRZ tethering complex. (A)** Rab18 interacted with NRZ complex. **(B and C)** Rab18 interacted with ZW10. **(D)** ZW10 interacted with GTP-bound Rab18 in vitro with a higher affinity. **(E)** ZW10 enhanced the interaction between Rab18 and NAG. Right: Schematic diagram showing the interaction pattern between Rab18 and NRZ complex. **(F)** The LD association of NAG and ZW10 was dependent on Rab18. Subcellular fractions were isolated from control or *Rab18*-deficient TM-3 cells. ADRP, GRP94, GM130, and β-tubulin represent LD, microsomal, Golgi, and cytosolic markers, respectively. **(G)** Colocalization of HA-Rab18 (pink), Cherry-ZW10 (red), and endogenous NAG (green) on LDs (blue). Bars: 10 µm; (insets) 2 µm. **(H)** Association of endogenous ZW10 (green) or endogenous NAG (green) with LDs (blue) in the presence of Rab18 (red). Bars: 10 µm; (insets) 2 µm. All experiments were performed at least twice. FL, full-length.

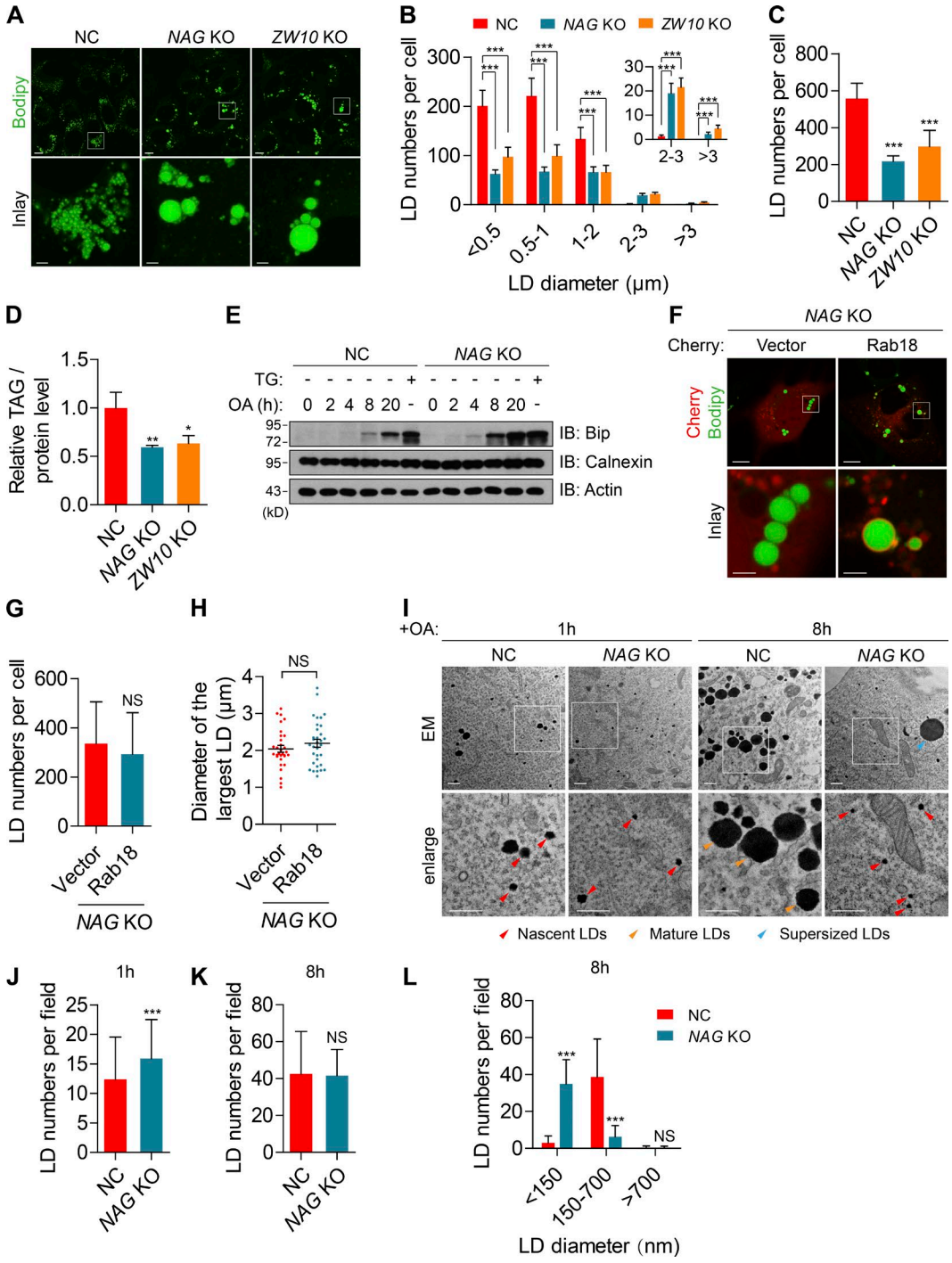

Figure 7. **NRZ complex acts as a downstream effector of Rab18 to control LD growth. (A–C)** Increased supersized LDs and reduced mature LDs in *NAG*-deficient (*NAG* KO) and *ZW10*-deficient (*ZW10* KO) 3T3-L1 preadipocytes. Bars: 10 μm; (insets) 2 μm. (B) The mean number of LDs in each diameter in A. (C) Quantification of the number of mature LDs per cell in A. Mean ± SD; $n = 13$ for control cells, $n = 22$ for *NAG*-deficient cells, $n = 20$ for *ZW10*-deficient cells; ***, $P < 0.001$ by one-way ANOVA with Tukey post hoc tests. **(D)** Reduced cellular TAG levels in *NAG* KO- and *ZW10* KO 3T3-L1 preadipocytes. Three independent experiments were performed. Mean ± SD; $n = 3$; *, $P < 0.05$; **, $P < 0.01$ by one-way ANOVA with Tukey post hoc tests. **(E)** Increased ER stress in *NAG KO* cells after long-term OA treatment (400 μM). Cells treated with 1 μM TG for 6 h were used as a positive control. **(F–H)** Introduction of Cherry-Rab18 (red) into *NAG* KO cells did not restore its function in the accumulation of mature LDs. (F) Representative images of LD morphology. LDs were stained with Bodipy 493/503. Green, LDs; red, Cherry. Bars: 10 μm; (insets) 2 μm. (G) Quantification of the number of mature LDs in each cell Mean ± SD; $n = 25$ cells for vector-transfected cells, $n = 27$ cells for Rab18-transfected cells; NS, no significance by Mann-Whitney test. (H) Quantification of the size of the largest LD in each cell Mean ± SEM; $n = 31$ cells for vector-transfected cells, $n = 33$ cells for Rab18-transfected cells; NS, no significance by two-tailed *t* test. **(I)** Representative EM images showing LD morphology in control and *NAG* KO 3T3-L1 preadipocytes. Bars, 500 nm. **(J)** The total number of LDs in each cell treated with OA for 1 h was increased. Mean ± SD; $n = 137$ ROIs for control cells, $n = 154$ ROIs for *NAG*-deficient cells; ***, $P < 0.001$ by Mann-Whitney test. **(K and L)** Defective LD growth and maturation in *NAG* KO cells treated with OA for 8 h. Number of LDs (K) and histogram of the mean number of LDs (L) in each diameter in cells treated with OA for 8 h in K. Mean ± SD; $n = 25$ ROIs for control cells, $n = 29$ ROIs for *NAG*-deficient cells; ***, $P < 0.001$; NS, no significance by Mann-Whitney test. All experiments were performed at least twice.

R-SNARE (that has an arginine at the center of its coiled-coil domain) are required to trigger typical membrane fusion, we isolated several potential R-SNAREs including Sec22b, Ykt6, and Vamp8 from LD fraction of the liver of *ob/ob* mice (Table S1). Knocking down Sec22b or Vamp8 did not affect LD morphology (Fig. 8, G and H). Knocking down Ykt6 led to a very minor effect in LD sizes and numbers (Fig. 8, G and H).

Consistent with its function in controlling LD growth, ER-associated Q-SNAREs were detected in the Rab18-IP complex (Fig. 8 I). Expression of Rab3GAP1/2 further enhanced the association of Rab18 with these SNAREs (Fig. 8 I). Biochemical fractionation showed that Stx18, Use1, and BNIP1 were all present in both ER and LD fractions in wild-type cells, but their presence in LD fraction was completely abolished in *Rab18*-deficient cells (Fig. 8 J). In addition, when Stx18, Use1, or BNIP1 was coexpressed with Rab18, they all showed in close proximity to LDs (Fig. 8 K). The LD association of ER-associated Q-SNAREs was dependent on the NRZ complex as *NAG* deficiency dramatically abolished their LD association (Fig. 9 A). GFP-Use1, when coexpressing with HA-Rab18, was recruited to LDs in 80% of wild-type cells, but its LD association was only observed in less than 20% *NAG*- or *ZW10*-deficient cells (Fig. 9, B and C). Surprisingly, Ykt6 interacted with neither Rab18 (Fig. 8 I) nor Stx18/Use1/BNIP1 Q-SNAREs (not depicted). In addition, it was not localized to LD, either (Fig. 8 J). Therefore, ER-associated Q-SNAREs are important in controlling LD growth and lipid storage by forming a complex with Rab18/NRZ tethering complex. The role of R-SNA RE Ykt6 in Rab18-mediated LD growth remains unclear.

Rab18/NRZ/SNARE complex establishes an ER–LD contact

As Stx18, Use1, and BNIP1 are ER membrane–integrated proteins, we hypothesize that the recruitment of these SNAREs to the LD surface may result in the recruitment of ER membrane to the LD surface to create a close contact between ER and LDs. Indeed, when CB5, an ER-specific protein, was coexpressed with Rab18 and BNIP1 in 3T3L1-preadipocytes, BNIP1-positive signals were almost completely colocalized with CB5 and Rab18 on the LD surface in approximately 80% of cells (Fig. 9, D and E), but in *NAG*-deficient cells the colocalization of CB5/BNIP1 (ER-positive) signals and Rab18 (LD-associated) signals was significantly abolished (observed in less than 20% of the cells; Fig. 9, D and E). The colocalization between ER and LD was also observed when another ER-specific protein, RFP-KDEL, was coexpressed with GFP-Use1 and HA-Rab18 (Fig. 9 F).

To directly visualize ER–LD contact, we coexpressed GFP-Stx18 and APEX-GBP (GFP binding protein) in wild-type, Rab18-overexpressing, and *Rab18*-deficient 3T3-L1 preadipocytes. As APEX catalyzes the formation of a high-electronic-density substance in the presence of DAB and OsO4 (Ariotti et al., 2015), the ER-localized Stx18 was observed as a higher density signal. Consistent with the fluorescent imaging analysis (Fig. 9, D and F), EM images showed that APEX-Stx18–positive ER cisternae were clearly observed in Rab18-overexpressing cells (Fig. 10 A). Moreover, multiple APEX-Stx18–positive signals were observed on the LD surface, indicating multiple direct contacts between ER and LD (Fig. 10 A, red arrows). Quantitative analysis showed that nearly 80% cells overexpressing Rab18 had at least one LD that was labeled with multiple condensed APEX-Stx18 signals (Fig. 10, A and B). Approximately 10% cells showed a single APEX-Stx18 positive signal on the LD surface in control wild-type cells, indicating a single ER–LD contact (Fig. 10, A and B). In *Rab18*-deficient cells, less than 2.5% cells contained such ER–LD contact (Fig. 10, A and B).

Furthermore, we also measured the presence of ER membrane near the LD surface (within the distance of 20 nm) as an indirect criterion of a potential ER–LD. In Rab18-overexpressing cells, nearly 60% LDs were apposed to ER membrane, and 33% of total LD surface area had ER membrane apposed to it. In control wild-type cells, ∼30% LDs showed ER apposition and 5% total LD surface area was apposed to ER membrane. In *Rab18*-deficient cells, less than 5% LDs showed ER apposition, and 1% of total LD surface area was apposed to ER membrane (Fig. 10, C and D). These data demonstrate that Rab18 controls a direct ER–LD contact and LD apposition to ER membrane.

Overall, our data indicate that Rab18 is able to recruit the NRZ protein complex and its associated ER–SNAREs to the close proximity of LD to form a close LD-ER contacting site that potentially enhances lipid transfer from ER to LD to promote LD growth.

Discussion

LDs serve as lipid storage depots, and their dynamic changes, including biogenesis and growth, are important in regulating lipid homeostasis. Here, we show that Rab18, a LD-associated RabGTPase, plays a key role in controlling LD growth and maturation by interacting with its effector, the NRZ/SNARE tethering protein complex, resulting in the initiation of close contact between ER and LD and facilitation of the incorporation of ER-synthesized lipids to LDs for their growth.

One of the most prominent features in *Rab18*-deficient fibroblast cells is the disappearance of normal-sized LDs and the appearance of a few supersized LDs. A similar role for Rab18 is also observed in mature adipocytes and in Leydig cells. *Rab18* deficiency in 3T3-L1 preadipocytes did not affect nascent LD biogenesis, lipolysis, FA uptake, and LD coalescence. TAG synthesis in *Rab18*-deficient 3T3-L1 preadipocytes was reduced. As we did not observe a difference in their expression levels and subcellular distribution of TAG synthesis enzymes in *Rab18*-deficient cells, the lower TAG synthesis may be a result of a secondary effect of defective LD growth. Rab18 was previously shown to control lipolysis in adipocytes (Pulido et al., 2011). We also observed a slight decrease in both basal and stimulated lipolysis in *Rab18*-deficient adipocytes. This is likely a result of a secondary effect of a decreased surface-to-volume ratio of LDs and the cellular TAG level. The formation of supersized LDs in *Rab18*-deficient cells may be a result of redirection of lipids from ER to a subset of LDs. Change of LD morphology was not observed in *Rab18*-deficient AML12, HeLa, Cos7, and 293T cells (unpublished data), indicating a cell type–specific role of Rab18 in controlling lipid storage and LD growth. Interestingly, although we observed similar expression levels of Rab18, Rab3GAP1/2, and NRZ/SNAREs in these cells to that in 3T3-L1 preadipocytes, the LD association of Rab18 was greatly enhanced in 3T3-L1 pre- and differentiated adipocytes and in Leydig cells (unpublished data). The distinct localization of Rab18 may account for its role in controlling LD growth and maturation. Alternatively, other RabGTPases may play a functionally redundant role in controlling LD growth in these cells.

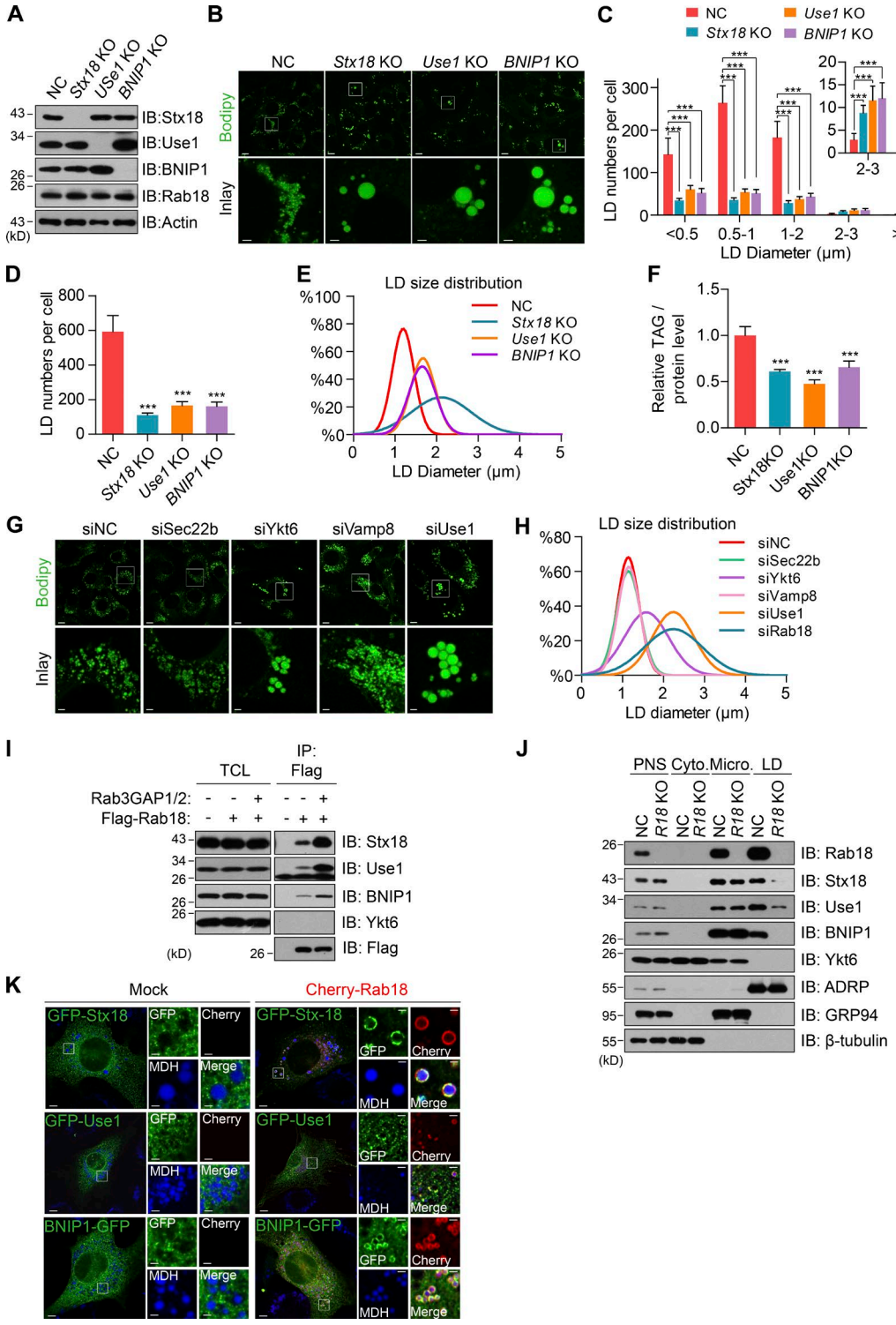

Figure 8. **ER-associated SNAREs control LD growth by interacting with Rab18/NRZ. (A–D)** KO ER-associated Q-SNAREs (Stx18, Use1, and BNIP1) in 3T3-L1 preadipocytes led to defective LD growth and the accumulation of supersized LDs. (A) Western Blot showing the expression level of indicated protein in 3T3-L1 preadipocytes. (B) Representative images of LD morphology. Bars: 10 μm; (insets) 2 μm. (C) Histogram showing the number of LDs in each diameter in B. (D) Quantification of the number of mature LDs in B. Mean ± SD; n = 15–20 for each genotype; ***, P < 0.001 by one-way ANOVA with Tukey post hoc tests. **(E)** The size distribution of the largest LD in each cell in B. The diameters of LDs from 218–252 cells/genotype (pooled from three experiments) were fitted with Gaussian function. **(F)** Reduced cellular TAG levels in *Stx18*-deficient, *Use1*-deficient, or *BNIP1*-deficient 3T3-L1 preadipocytes. Three independent experiments were performed. Mean ± SD; n = 3; ***, P < 0.001 by one-way ANOVA with Tukey post hoc tests. **(G)** LD morphology in 3T3-L1 preadipocytes knocking down R-SNAREs (Sec22b, Ykt6, and Vamp8). Green, LDs. Bars: 10 μm; (insets) 2 μm. **(H)** The LD size distribution in G. The diameters of LDs from 97–206 cells/genotype (pooled from three experiments) were fitted with Gaussian function. **(I)** Rab18 interacts with ER-associated Q-SNAREs. **(J and K)** The LD association of ER-associated Q-SNAREs is dependent on Rab18 by biochemical fractionation (J) and imaging (K) analyses. Subcellular fractions were isolated from control or *Rab18* KO TM-3 cells. In K, Q-SNAREs, LD, and Cherry-Rab18 were labeled green, blue, and red, respectively. Bars: 10 μm; (insets) 2 μm. All experiments were performed at least twice.

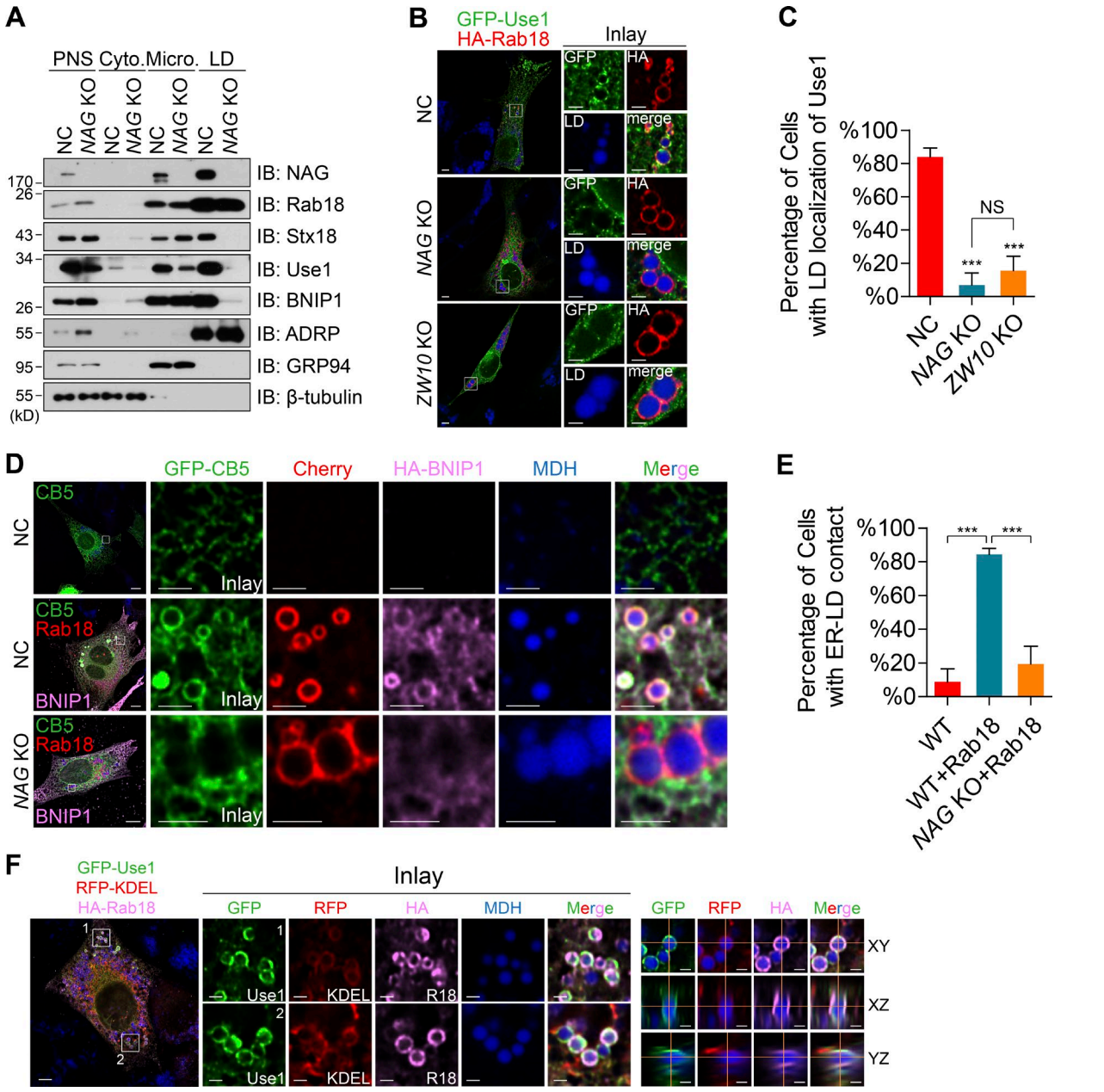

Figure 9. **Rab18/NRZ/SNARE complex establishes ER–LD contact. (A)** Presence of ER-associated SNAREs in LD fraction is dependent on NAG. Subcellular fractions were isolated from control or *NAG* KO 3T3-L1 preadipocytes. **(B and C)** Use1 (green) was colocalized with Rab18 (red) to LDs (blue) in the control but not in *NAG* KO or *ZW10* KO 3T3-L1 preadipocytes. Bars: 5 µm; (insets) 2 µm. (C) Quantitative analysis. Cells with Rab18 were selected for calculation and LDs with GFP-Use1 localization were counted as positive. Three independent experiments were performed. Mean ± SD; $n = 3$; ***, $P < 0.001$; NS, no significance by one-way ANOVA with Tukey post hoc tests. **(D)** Colocalization of CB5 (green, an ER-associated protein), Rab18 (red), and BNIP1 (pink) on LDs in wild-type but not in *NAG* KO cells. Bars: 10 µm; (insets) 2 µm. **(E)** Quantification of percentage of cells containing CB5 positive LDs in D. Rab18-positive cells were selected for calculation. Three independent experiments were performed. Mean ± SD; $n = 3$; ***, $P < 0.001$ by two-tailed *t* test. **(F)** Colocalization of GFP-Use1 (green), RFP-KEDL (red, an ER-specific marker) and HA-Rab18 (pink) on LDs. 3D view of indicated channels are shown in xy, xz, or yz direction. Bars: 10 µm; (insets) 2 µm. All experiments were performed at least twice.

The LD localization and activity of Rab18 is controlled by its GEFs, Rab3GAP1/2, as Rab3GAP1/2 is colocalized with Rab18 on LDs and their depletion abolishes the LD association of Rab18 and results in the loss of mature LDs and reduction in lipid storage. As Rab3GAP1/2 is also shown to be responsible for the ER localization of Rab18 in COS7 cells and may regulate ER tubulation (Gerondopoulos et al., 2014), the localization and function of Rab18 and its GEF could be cell type dependent.

Importantly, we found that the GTP-bound form of Rab18 interacts directly with the C-terminal region of ZW10, one of the subunits of the NRZ tethering factors. In addition, NRZ complex and its associated Q-SNAREs form a protein complex with Rab18. Therefore, ZW10 acts as a bridge to recruit the NRZ tethering complex and its associated Q-SNAREs to Rab18. Functionally, NRZ and its associates, Q-SNAREs, act downstream of Rab18 to control LD growth, lipid storage, and FA-overloading–induced ER stress, almost a complete recapitulation of the role

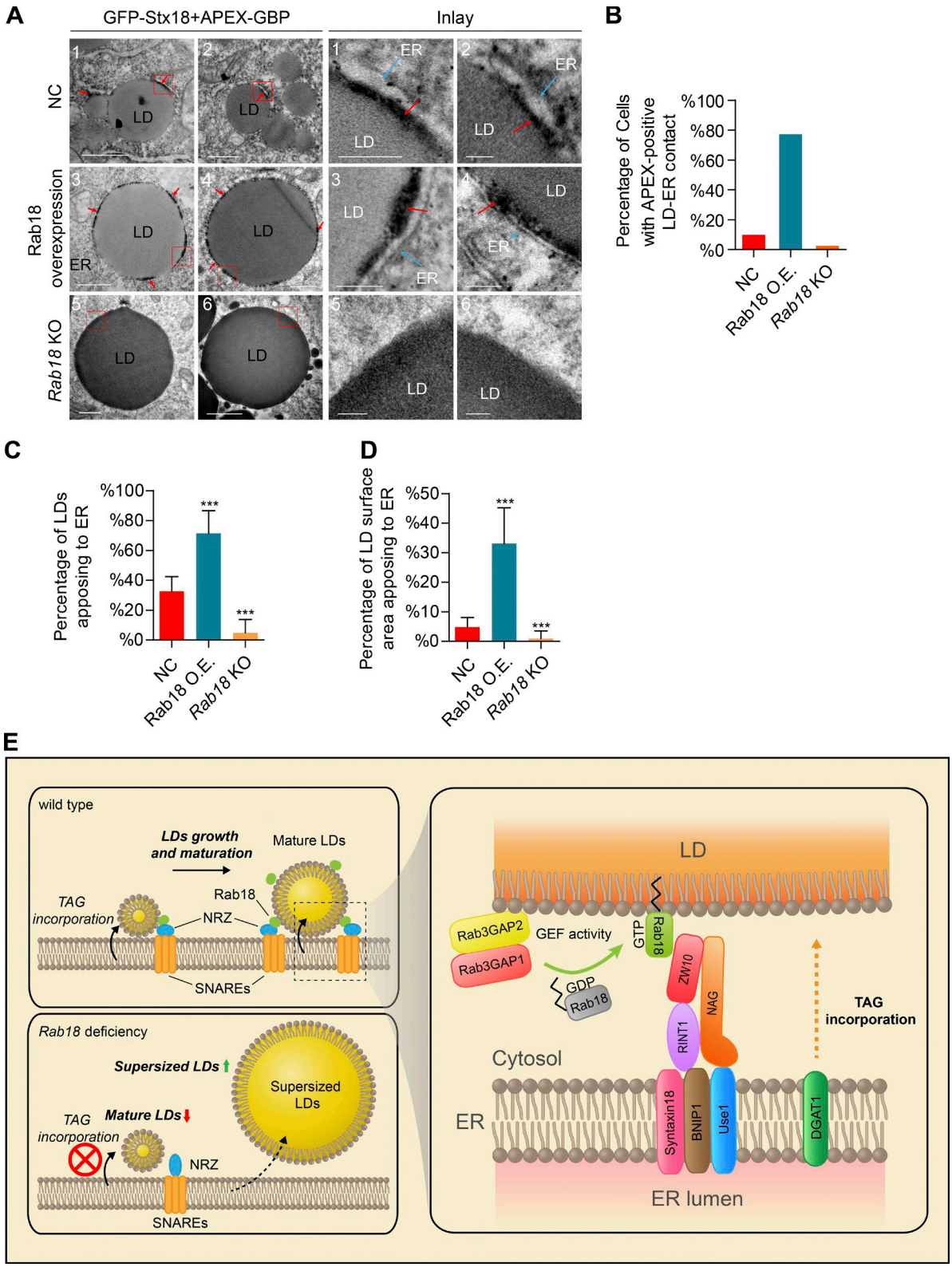

Figure 10. **Tethering LDs to ER by Rab18/NRZ/SNARE complex controls LD growth. (A)** Representative EM images showing a close contact between ER and LD in Rab18 overexpressing cells. ER cisternae are indicated with blue arrow; ER–LD contact sites are indicated with red arrows. Bars: (1–5) 500 nm; (6) 1 µm; (insets) 100 nm. **(B)** Quantification of percentage of cells containing APEX-Stx18–positive ER–LD contact (22–39 cells/genotype, pooled from two experiments). **(C)** Quantification of percentage of LDs apposing to ER per ROI. Mean ± SD; n = 11–17 ROIs/genotype; ***, $P < 0.001$ by two-tailed t test. **(D)** Quantification of percentage of LD surface area apposing to ER per ROI. Mean ± SD; n = 11–17 ROIs/genotype; ***, $P < 0.001$ by Mann-Whitney test. **(E)** Working model: Rab18-GTP binds to the NRZ tethering complex and its associated Q-SNAREs to recruit ER to the close proximity of LDs to create a contact between ER and LDs, allowing the transfer of TAG from ER to LDs at the interface of ER–LD to promote nascent LD growth. All experiments were performed at least twice. O.E., overexpression.

of Rab18. Unlike the membrane fusion mediated by Q-SNAREs and R-SNARE, thus far, a typical R-SNARE in Rab18-mediated LD growth has not yet identified. Ykt6 appears to have a very minor effect in Rab18-mediated LD sizes, but it was not localized to LDs and did not interact with Rab18 either (Fig. 8, I and J). This minor effect of Ykt6 may be a result of its regulatory role in controlling the assembly and association of ER-associated SNA REs with the NRZ complex. A similar role of Ykt6 has been observed in Golgi-ER retrograde transport (Meiringer et al., 2011).

Mechanistically, interaction between LD-associated Rab18, NRZ tethering complex, and ER-associated Q-SNAREs is able to bring LD and ER within close proximity. We have several pieces of evidence to support this. First, our biochemical fractionation analysis showed that NRZ proteins and ER-associated Q-SNAREs are present in LD fraction in the presence of Rab18. Second, fluorescent imaging analysis indicates that NRZ and Q-SNAREs are colocalized with Rab18 on the LD surface. Finally and most important, EM analysis using the APEX staining technique clearly demonstrated that in the presence of Rab18, ER membrane is in close contact with LDs to form special ER–LD contact sites. This is consistent with previous observation that overexpression of Rab18 causes an enwrapping of LD by ER membrane (Ozeki et al., 2005).

The cross talk between ER and LD in regulating LD growth and maturation has been observed in yeast, where nascent LDs seem to be constantly connected with the ER (Jacquier et al., 2011) in *Caenorhabditis elegans* (Xu et al., 2012b) and in hepatocytes where ApoB is shown to tightly associate with the LDs (Ohsaki et al., 2008). ER–LD contact is also observed in seipin-mediated LD growth (Salo et al., 2016; Wang et al., 2016). But the precise molecular nature of such contact remains unclear.

What is the precise mechanism of Rab18-NRZ-SNAREs in controlling lipid incorporation from ER to LDs for their growth? According to the crystal structure of Dsl1 and the speculated structure of NRZ tethering complex (Ren et al., 2009), we postulate that when Rab18-GTP binds to the ZW10 subunit that is localized on the top of the NRZ "rod," it will bind to ER-associated SNAREs, resulting in the assembly of Rab18-NRZ-SNARE complex. Assembly of Rab18-NRZ-SNARE complex results in the tethering of ER membrane to LDs to create a direct ER–LD contact. In addition, Rab18-NRZ-SNARE complex assembly may provide energy for the subsequent deformation of ER bilayer and LD monolayer membrane, resulting in a direct transfer of TAG synthesized from ER to LDs at the ER and LD interface to promote nascent LD growth. Alternatively, Rab18-NRZ-SNARE complex may control phospholipid dynamics or composition in ER–LD interface to facilitate the distribution of TAG from ER to LDs (Fei et al., 2011; Ben M'barek et al., 2017). Finally, Rab18-NRZ-SNARE complex assembly may allow the recruitment of other proteins to the ER–LD contact site to form a special channel or pore to allow the incorporation of lipids from ER to LDs (Fig. 10 E). The delineation of the Rab18-NRZ-SNARE regulatory loop holds great promise for them to be molecular targets for developing therapeutic drugs for lipid storage–related diseases.

Materials and methods

DNA construction and reagents

Full-length cDNAs encoding various mouse proteins were amplified by PCR from cDNAs of 3T3-L1 preadipocytes or mouse liver. cDNA encoding mouse Rab18 was cloned into pCMV5-HA (Clontech), pCMV5-Flag (Clontech), pEGFP-C1 (Clontech), pmCherry-C1 (Clontech), or pGEX-6P-1 (GE Healthcare) vectors. Point mutations of Rab18 were introduced by a PCR-based site-directed mutagenesis. *LiveDrop* LD marker was generated by cloning sequences encoding the hairpin domain of mouse GPAT4 into pEGFP-N1 (Clontech) vector, according to previous description (Wang et al., 2016). GFP-CB5 was generated by cloning sequences encoding the C-terminal transmembrane domain of mouse Cytb5 into pEGFP-C1 vector. cDNA encoding mouse GPAT4 was cloned into pEGFP-N1 vector. cDNAs encoding mouse GPAT3, DGAT1, and DGAT2 were constructed into pEGFP-C1 vector. cDNAs encoding mouse Rab3GAP1 and Rab3GAP2 were cloned into pCMV5-HA or pCMV5-Flag vectors. cDNAs encoding mouse ZW10 and RINT1 were cloned into pEGFP-C1, pCMV5-HA, or pCMV5-Flag vectors. Full-length cDNA encoding human NAG was amplified from cDNA libraries provided by Jiahuai Han (Xiamen University, Xiamen, China) and cloned into pCDNA 3.1(-)-Flag (Invitrogen), pCMV5-HA, or pEGFP-C1 vectors. Truncations of NAG encoding amino acids 734–1355 (Sec39 domain) and 1356–2371 were subcloned into pCDNA3.1(-)-Flag vector. cDNAs encoding Stx18 and Use1 were cloned into pEGFP-C1 vector. cDNA encoding mouse BNIP1 was cloned into pEGFP-N1 vector.

DGAT1 inhibitor (PF-04620110) was purchased from Selleck Chemicals. OAs, TG, free glycerol reagent, triglyceride reagent, isoproterenol, IBMX, DGAT2 inhibitor (PF-06424439), M2-agarose beads, glutathione, and 3×Flag peptide were purchased from Sigma-Aldrich. Protease inhibitor cocktail tablet and protein G agarose beads were purchased from Roche. Glutathione agarose beads were from GE Healthcare. Free fatty acid (FFA) uptake kit was from Abcam. Bodipy 493/503, Bodipy C12, LipidTOX neutral red, and LipidTOX deep red were from Life Technologies. Monodansylpentane (MDH) was obtained from Abgent.

Antibodies

Antibodies against Fsp27 were described previously (Sun et al., 2013a; Wu et al., 2014a). Antibodies against HA (mouse, sc-7392), Flag (mouse, sc-807), GFP (rabbit, sc-8334), GRP94 (rat, sc-32249), RINT1 (goat, sc-19404), Syntaxin18 (mouse, sc-293067), and BNIP1 (goat, sc-1713) were purchased from Santa Cruz Biotechnology. Antibodies against Rab10 (rabbit, 4262), FABP4 (rabbit, 3544) and Bip (rabbit, 3177) were obtained from Cell Signaling Technology. Antibodies against NAG (rabbit, ab122370; used for Western blot) and ZW10 (rabbit, ab21582; used for immunofluorescence [IF]) were obtained from Abcam. Antibodies against Rab3GAP1 (rabbit, HPA034495); Rab3GAP2 (rabbit, HPA026273), NAG (rabbit, HPA036817; used for IF), Use1 (rabbit, HPA047562), and Ykt6 (rabbit, HPA030817) were obtained from Human Protein Atlas. Antibodies against Rab18 (mouse, 60057–1-Ig; used for IF) and ZW10 (rabbit, 24561–1-AP; used for Western blot) were obtained from Proteintech. Antibody against ACSL3 (mouse, H00002181-B0) was obtained from Abnova. Antibodies against Rab18 (rabbit, SAB4200173, used for Western blot), Calnexin (rabbit, C4731), β-tubulin (mouse, T0198), and actin (mouse, A5441) were purchased from Sigma-Aldrich. Antibodies against ADRP (guinea pig, 20R-Ap002) and Plin1 (guinea pig, 20R-pp004) were purchased from Fitzgerald Industries. Antibody against GM130 (mouse, 610822) was obtained from BD Bioscience. Antibody against GST (mouse, AB101) was obtained from Tiangen. HRP-conjugated goat anti–mouse or rabbit IgG was obtained from GE Healthcare. Alexa Fluor 488/568/647–conjugated donkey anti–mouse or rabbit IgG was purchased from Life Technologies.

Cell culture and transfection

293T cells (CRL-3216; ATCC) and 3T3-L1 preadipocytes (CL-173; ATCC) were cultured in high-glucose DMEM (Life Technologies)

containing 10% FBS (Life Technologies), 2 mM L-glutamine, 100 U/ml penicillin, and 100 µg/ml streptomycin at 37°C in a humidified incubator containing 5% CO_2. TM-3 Leydig cells were obtained from ATCC (CRL-1714) and cultured in high-glucose DMEM supplemented with 5% FBS and 2.5% horse serum. Monolayers of 3T3-L1 preadipocytes were induced to differentiate into mature adipocytes as described by the protocol of ATCC.

Plasmid DNAs were transfected into 293T cells using Lipofectamine 2000 according to the manufacturer's instructions (Invitrogen). Electroporation of 3T3-L1 preadipocytes and mature adipocytes was performed using Amaxa Nucleofector II (Lonza) with program A-033 according to the manufacturer's instructions.

RNA interference

siRNAs were introduced into 3T3-L1 preadipocytes by electroporation as described in the Cell culture and transfection section. Cells were then cultured for 48 h and harvested. The knockdown efficiency for each protein was evaluated by semiquantitative real-time PCR analysis or Western blot analysis. siRNAs used in all experiments are listed in Table S2.

Generation of KO cell line using CRISPR/Cas9

Generation of KO cell lines was performed according to previous studies (Ran et al., 2013; Cao et al., 2016). In brief, single guide RNAs (sgRNAs) were designed using CHOPCHOP (https://chopchop.rc.fas.harvard.edu/) and constructed into pLentiCRISPRv1 vector (49535; AddGene). *Lentivirus* were produced by cotransfecting pLentiCRISPRv1 with packaging plasmids pMD2.G (12259; AddGene) and psPAX2 (12260; AddGene) into 293T cells. Purification of *Lentivirus* was performed as previously described (Nian et al., 2010). 3T3-L1 preadipocytes or TM-3 Leydig cells were infected with *Lentivirus* for 24 h, and were treated with 2 µg/ml of puromycin for 4–5 d to select positive clones. The drug-resistant cells were then diluted and plated on 96-well dishes to form a single colony. KO efficiency of each cell line was determined by Western blot analysis. Genomic edition was finally validated by sequencing the genomic sequence flanking the targeting sites that were amplified using PCR and subcloned to pEASY-T1 (Transgene). sgRNAs used for knocking out various genes are shown in Table S3.

Immunostaining

For immunostaining, cells cultured on coverslips were washed twice with PBS, fixed with 4% paraformaldehyde for 20 min, and permeabilized with 0.1% saponin for 20 min. Cells were blocked with 10% goat serum in PBS supplemented with 0.1% saponin for 1 h and incubated with primary antibodies (1:50–1:200 diluted) in PBS supplemented with 0.1% saponin overnight at 4°C and then with secondary antibodies (1:500 diluted) for 1 h at room temperature. LDs were stained with Bodipy 493/503 (1:200 diluted), LipidTOX (1:300 diluted), or MDH (1:500 diluted) in PBS for another 20 min.

Fluorescent imaging

Images were collected on a Nikon A1R+ laser scanning confocal microscope with CFI Plan Apo 100× oil immersion objective (NA 1.45) and 405/488/561/640 laser. GaAsP multidetector photomultiplier tube was used to obtain images. For fixed cells, images were acquired at room temperature. Images with 1024 × 1024 pixels were obtained with 4 frames mean. For z-stack images, images (1,024 × 1,024 pixels) with 0.3 µm per section were obtained. Living cell imaging was performed according to a previous study (Sun et al., 2013b). Cells were cultured in a living cell station (Oko Lab) at 37°C, 5% CO_2, and 80% humidity. After loading with 200 µM OA (with 1:1,000 diluted Bodipy 493/503 or LipidTOX neutral red), images (512 × 512 pixels) were taken in 2-min intervals for 8 h. For 3D time-lapse imaging, optical sections were obtained with 0.3-µm thickness in every 30 min. NIS-Element software (Nikon) was used to obtain images.

Structured illumination microscopy (SIM) images were obtained using a Nikon N-SIM superresolution microscope with SR Plan Apo 100× oil immersion objective (NA 1.49) and Andor iXon 897 EMC CD at room temperature.

Transmission electron microscopy

Cells were fixed in 2.5% gluteraldehyde in 0.1 M sodium cacodylate buffer, pH 7.4, for 1 h and washed with 0.1 M sodium cacodylate buffer. Cells were then postfixed with 1% OsO_4, 1.5% potassium ferrocyanide, and 1 mM $CaCl_2$ in 0.1 M sodium cacodylate buffer. Next, the cells were dehydrated in a graded series of ethanol, substituted with propylene oxide, and infiltrated with the SPON12 resin mixture followed by polymerization at 60°C for 24 h. Ultrathin sections were prepared using Lecia Ultracut R. Samples were observed using a Hitachi H-7650 transmission electron microscopy at 80 kV.

APEX-EM and quantification

APEX-EM was performed according to the method described in Ariotti et al. (2015) and Lam et al. (2015). In brief, cells were washed 3 times with 0.1 M sodium cacodylate buffer, and then washed with 1 mg/ml DAB/cacodylate mixture for 2 min. Sodium cacodylate buffer supplied was 1 mg/ml DAB and 5.88 mM H_2O_2 were added to the cells for 30 min at room temperature. After that, the cells were washed three times with 0.1 M sodium cacodylate buffer and postfixed with 1% OsO_4 in 0.1 M cacodylate buffer for 2 min.

For quantitative analysis of the percentage of cells containing APEX-Stx18–labeled ER–LD contact, 22–39 cells/genotype were randomly selected. A cell that had at least one LD containing APEX-Stx18 signal on its surface was counted as positive.

For quantitative analysis of the percentage of LDs apposing to ER, 11–17 regions of interest (ROIs) from 11–17 cells were randomly selected, and 143–363 LDs were evaluated for wild-type, Rab18-overexpressing, and *Rab18*-deficient cells. An LD that was closely apposing to ER cisternae (within a distance of less than 20 nm) was counted as positive. For quantitative analysis of the percentage of LD surface area apposing to ER, 11–17 ROIs were randomly selected from 11–17 cells per genotype (143–363 LDs). The length of LD surface apposing to ER and LD circumference was measured using ImageJ-FIJI. For each LD in a ROI, the ratio of the length of LD-ER apposition to the LD circumference was calculated and averaged.

Image processing and analysis

Images were processed in NIS-element or ImageJ. Deconvolution of fluorescent images in Fig. 5 C; Fig. S3 (A and I); Fig 6 (G and H); Fig. S4 D; Fig. 8 K; and Fig. 9 (B, D, and F) was performed in NIS-element. The diameters of the largest LD per cell were measured through NIS-element or ImageJ. LD numbers per field and the diameter of LDs in EM images were determined using NIS-element. 3D surface reconstitution of LDs was performed in Imaris 8.0 (Bitplanet). LDs stained with fluorescent dyes were detected in surface mode using background subtraction method, and the numbers, sizes, and volumes of LDs were automatically measured.

Measurement of cellular TAG

Cells were loaded with 200 µM OA for 20 h and harvested. Cells were scraped from dishes, washed with PBS, and lysed in lipid extraction solution (hexane/isopropanol 3:2, vol/vol). After centrifugation at 1,000 *g* for 5 min, the upper organic phase was collected and dried

with nitrogen gas. Lipids were resuspended in chloroform containing 1% Triton X-100 and then dried with nitrogen gas. Lipids were finally resuspended in water. TAG level was measured using TAG reagent (Sigma-Aldrich) and free glycerol reagent (Sigma-Aldrich).

FFA uptake assay

FFA uptake rate was measured using the Free Fatty Acid Uptake Assay kit (Abcam). In brief, 3T3-L1 preadipocytes were serum-starved for 1 h, and then incubated with FA dye-loading solution for 10 min. Fluorescence signals were measured using a microplate reader with FITC filter (PerkinElmer).

Measurement of lipolysis rates

3T3-L1 preadipocytes were loaded with 200 µM OA and 1 µCi/ml [^{3}H]-OA overnight. Cells were rinsed twice with opti-MEM and cultured in opti-MEM containing 1% FA–free BSA for 2 h at 37°C. FA released was extracted from medium and measured using a MicroBeta Jet (PerkinElmer) liquid scintillation counter.

For lipolysis assay of mature adipocytes, 8-d differentiated 3T3-L1 adipocytes were washed three times with PBS and then incubated in phenol red–free, serum-free DMEM (Gibco) containing 1% fatty acid–free BSA (Sigma-Aldrich) in the presence or absence of 10 mM isoproterenol and 10 mM IBMX for 4 h. The amount of glycerol released into culture medium was measured by free glycerol reagent (Sigma-Aldrich).

Measurement of lipid synthesis rates

3T3-L1 preadipocytes were serum starved overnight, and then incubated with 200 µM OA and 1 µg/ml Bodipy C12 for 0, 30, 60, and 120 min before harvesting. Lipids were extracted using chloroform/methanol (2:1, vol/vol), loaded onto TLC plates, and separated with hexane/diethyl ether/acetate (70:30:1, vol/vol). The TLC plate was scanned by Typhoon trio+ (GE Healthcare) and the fluorescent intensity of TAG spots was measured in ImageJ.

Protein expression and purification

GST-Rab18 was purified from *E. coli* strain BL21 (DE3). Bacteria that were transformed with pGEX-6p-1-Rab18 were grown in LB medium containing 100 µg/ml ampicillin to OD 0.6, and induced with 0.01 mM IPTG for 12 h at 16°C. Cells were harvested, resuspended, and then lysed in lysis buffer (25 mM Tris, pH 7.4, 150 mM NaCl, 1% Triton X-100, 1 mM PMSF, 1 mM DTT, and 10% glycerol) by sonication. Recombinant protein was first purified using Glutathione Sepharose 4B (GE Healthcare) according to the manufacturer's instructions. Proteins were concentrated and further purified by gel filtration chromatography (Superdex 200 10/300 GL; GE Healthcare) in 20 mM Tris, pH 7.4, 100 mM NaCl, 1 mM $MgCl_2$, and 1 mM DTT.

Flag-ZW10 was purified from 293T cells. 8 µg of pCMV5-flag-ZW10 plasmid was introduced into each 10-cm dish of 293T cells for 24 h. Cells were scraped from dishes and washed with PBS. Cells were resuspended in lysis buffer (20 mM Tris, pH 7.4, 150 mM NaCl, 1 mM EDTA, and 0.4% CHAPS), supplemented with protease inhibitor cocktail (Roche), and then broken by sonication. Cell lysates were spun at 12,000 *g*, and the supernatants were incubated with M2 beads for 3 h at 4°C. The beads were washed with washing buffer five times (20 mM Tris, pH 7.4, 700 mM NaCl, 5 mM EDTA, and 0.4% CHAPS), and the protein was eluted with elution buffer (20 mM Tris, pH 7.4, 100 mM NaCl, and 100 µg/ml 3×flag peptide).

Protein concentration was determined using the Bradfold method (Bio-Rad). The purity of protein was evaluated with Coomassie Brilliant Blue (Sigma-aldrich) staining or silver staining.

IP

For IP, cellular protein was extracted with IP buffer (20 mM Tris, pH 7.4, 100 mM NaCl, 1 mM $MgCl_2$, and 0.4% CHAPS), supplemented with protease inhibitor cocktail (Roche). After being centrifuged at 12,000 *g*, the supernatants were incubated with M2 beads to pull down flag-tagged protein for 3 h at 4°C. The beads were washed with IP buffer three times before adding 1.2× laemmli loading buffer. Proteins co-IP were analyzed by Western blot. For IP of endogenous protein, antibody or preimmune serum premixed with protein G beads (Roche) was used.

For in vitro binding assay, 1.5 µg GST protein or 2.5 µg GST-Rab18 was loaded with 1 mM GTP-γS or 1 mM GDP in nucleotide loading buffer (20 mM Tris, pH 7.4, 100 mM NaCl, 1 mM $MgCl_2$, 5 mM EDTA, and 0.4% CHAPS) for 1 h at 4°C, followed by adding 10 mM $MgCl_2$ to stop reaction for 10 min on ice. Next, 2 µg flag-ZW10 prebound to M2 beads was added to form protein complex with GST-Rab18 for 2 h at 4°C. The beads were then washed with washing buffer (20 mM Tris, pH 7.4, 150 mM NaCl, 10 mM $MgCl_2$, and 0.4% CHA PS) three times before the addition of 1.2× laemmli loading buffer.

Subcellular fractionation

Subcellular fractionation was performed according to the method described in Ding et al. (2013) and Gong et al. (2011) with slight modifications. TM-3 cells were harvested, washed with PBS, and resuspended in hypotonic buffer (10 mM Hepes, pH 7.8, 1 mM EGTA, and 25 mM KCl) for 20 min on ice. Cells were spun down at 600 *g* for 5 min, and the supernatants were discarded. Cells were resuspended with TES buffer (20 mM Tris, pH 7.4, 1 mM EDTA, and 250 mM sucrose) and homogenized through Dounce homogenizer (Kimble Chase) with loose pestle 25 times. The postnuclear supernatants (PNSs) were obtained after centrifugation at 1,000 *g* for 10min. PNS was further centrifuged at 12,000 *g* for 15 min to get postmitochondrial fraction. Floating buffer (100 mM NaCl, 20 mM Tris, pH 7.4, and 1.5 mM $MgCl_2$) was laid on postmitochondrial fraction and centrifuged at 200,000 *g* for 1 h using a Beckmann SW41 rotor. The pellet fraction and middle gradient were collected as crude microsomal fraction and cytosol, respectively. The LDs on the top were collected and washed three times with floating buffer. All procedures were performed at 4°C, and protease inhibitors were added. Protein concentration was determined using BCA assay (Thermo Fisher Scientific). Relative amounts of protein on each fraction were analyzed by Western blot.

Statistics

Data were subjected to statistical analysis and plotted using Graphpad Prism 5.0. Statistical calculations to predetermine required sample size were not performed. The D'Agostino and Pearson omnibus normality test was used to determine the normal distribution of data. For data with normal distribution, single comparisons were performed using the two-tailed Student's *t* test, whereas multiple comparisons were assessed by one-way ANOVA with the Tukey post hoc test. Dataset that did not follow normal distribution were analyzed using nonparametric tests (Mann-Whitney test for single comparisons or Kruskal-Wallis test for multiple comparisons). For all analyses, a p-value <0.05 was considered to be statistically significant. Results are reported either by mean ± SEM or mean ± SD as indicated in the figure legends. The methods for calculating p-values are indicated in the figure legends.

Online supplemental material

Fig. S1 shows defective LD growth and maturation in *Rab18*-deficient cells (related to Fig. 1). Fig. S2 shows that TAG synthesis on ER is required for Rab18-controled LD growth (related to Fig. 4). Fig. S3 shows that Rab3GAP1/2 controls the activity and LD localization of

Rab18 (related to Fig. 5). Fig. S4 shows that Rab18 binds to NRZ tethering complex (related to Fig. 6). Fig. S5 shows that NRZ complex acts as a downstream effector of Rab18 to control LD growth (related to Fig. 7). Video 1 shows the time course of LD accumulation in control cells. Video 2 shows the time course of LD accumulation in Rab18 knocked down cells. Video 3 showstime-lapse 3D images of LD accumulation in control cells. Video 4 shows time-lapse 3D images of LD accumulation in Rab18 knocked down cells. Video 5 shows time-lapse 3D images of LD accumulation in control cells. Video 6 shows time-lapse 3D images of LD accumulation in *NAG*-deficient cells. Table S1 shows SNAREs identified from LD fraction isolated from hepatocytes of ob/ob mice. Table S2 shows siRNAs used in this work. Table S3 shows sgRNAs used in this work.

Acknowledgments

We thank members of the P. Li Laboratory at Tsinghua University for helpful discussion, and the Center of Biomedical Analysis at Tsinghua University and the Centre for Microscopy and Microanalysis at the University of Queensland for scientific and technical assistance.

This work was supported by grants from the National Natural Science Foundation of China (31690103 and 31430040) to P. Li, the National Key R&D Program of China (2016YFA0502002) to P. Li, the National Health and Medical Research Council, Australia (569542, 1045092, and 1037320), to R.G. Parton, and the National Natural Science Foundation of China (31621063) to P. Li. H. Yang is a Senior Research Fellow of the National Health and Medical Research Council, Australia.

The authors declare no competing financial interests.

Author contributions: D. Xu and L. Wu designed experiments. D. Xu, Yuqi Li, and L. Wu performed the majority of experiments with the help of D. Zhao, J. Yu, and T. Huang. D. Xu, Ying Li, C. Ferguson, and R.G. Parton performed the EM analysis. H. Yang and R.G. Parton participated in results discussion and manuscript preparation. P. Li supervised the entire project and was responsible for finalizing and submitting the manuscript.

Submitted: 29 April 2017
Revised: 12 October 2017
Accepted: 22 December 2017

References

Aligianis, I.A., C.A. Johnson, P. Gissen, D. Chen, D. Hampshire, K. Hoffmann, E.N. Maina, N.V. Morgan, L. Tee, J. Morton, et al. 2005. Mutations of the catalytic subunit of RAB3GAP cause Warburg Micro syndrome. *Nat. Genet.* 37:221–223. https://doi.org/10.1038/ng1517

Anand, P., S. Cermelli, Z. Li, A. Kassan, M. Bosch, R. Sigua, L. Huang, A.J. Ouellette, A. Pol, M.A. Welte, and S.P. Gross. 2012. A novel role for lipid droplets in the organismal antibacterial response. *eLife.* 1:e00003. https://doi.org/10.7554/eLife.00003

Andag, U., T. Neumann, and H.D. Schmitt. 2001. The coatomer-interacting protein Dsl1p is required for Golgi-to-endoplasmic reticulum retrieval in yeast. *J. Biol. Chem.* 276:39150–39160. https://doi.org/10.1074/jbc.M105833200

Arasaki, K., M. Taniguchi, K. Tani, and M. Tagaya. 2006. RINT-1 regulates the localization and entry of ZW10 to the syntaxin 18 complex. *Mol. Biol. Cell.* 17:2780–2788. https://doi.org/10.1091/mbc.E05-10-0973

Ariotti, N., T.E. Hall, J. Rae, C. Ferguson, K.A. McMahon, N. Martel, R.E. Webb, R.I. Webb, R.D. Teasdale, and R.G. Parton. 2015. Modular Detection of GFP-Labeled Proteins for Rapid Screening by Electron Microscopy in Cells and Organisms. *Dev. Cell.* 35:513–525. https://doi.org/10.1016/j.devcel.2015.10.016

Bem, D., S. Yoshimura, R. Nunes-Bastos, F.C. Bond, M.A. Kurian, F. Rahman, M.T. Handley, Y. Hadzhiev, I. Masood, A.A. Straatman-Iwanowska, et al. 2011. Loss-of-function mutations in RAB18 cause Warburg micro syndrome. *Am. J. Hum. Genet.* 88:499–507. https://doi.org/10.1016/j.ajhg.2011.03.012

Ben M'barek, K., D. Ajjaji, A. Chorlay, S. Vanni, L. Foret, and A.R. Thiam. 2017. ER Membrane Phospholipids and Surface Tension Control Cellular Lipid Droplet Formation. *Dev. Cell.* 41:591–604.

Binns, D., S. Lee, C.L. Hilton, Q.X. Jiang, and J.M. Goodman. 2010. Seipin is a discrete homooligomer. *Biochemistry.* 49:10747–10755. https://doi.org/10.1021/bi1013003

Burri, L., O. Varlamov, C.A. Doege, K. Hofmann, T. Beilharz, J.E. Rothman, T.H. Söllner, and T. Lithgow. 2003. A SNARE required for retrograde transport to the endoplasmic reticulum. *Proc. Natl. Acad. Sci. USA.* 100:9873–9877. https://doi.org/10.1073/pnas.1734000100

Cao, J., L. Wu, S.M. Zhang, M. Lu, W.K. Cheung, W. Cai, M. Gale, Q. Xu, and Q. Yan. 2016. An easy and efficient inducible CRISPR/Cas9 platform with improved specificity for multiple gene targeting. *Nucleic Acids Res.* 44:e149.

Cartwright, B.R., and J.M. Goodman. 2012. Seipin: from human disease to molecular mechanism. *J. Lipid Res.* 53:1042–1055. https://doi.org/10.1194/jlr.R023754

Chitraju, C., N. Mejhert, J.T. Haas, L.G. Diaz-Ramirez, C.A. Grueter, J.E. Imbriglio, S. Pinto, S.K. Koliwad, T.C. Walther, and R.V. Farese Jr. 2017. Triglyceride Synthesis by DGAT1 Protects Adipocytes from Lipid-Induced ER Stress during Lipolysis. *Cell Metab.* 26:407–418.

Choudhary, V., N. Ojha, A. Golden, and W.A. Prinz. 2015. A conserved family of proteins facilitates nascent lipid droplet budding from the ER. *J. Cell Biol.* 211:261–271. https://doi.org/10.1083/jcb.201505067

Diefenbacher, M., H. Thorsteinsdottir, and A. Spang. 2011. The Dsl1 tethering complex actively participates in soluble NSF (N-ethylmaleimide-sensitive factor) attachment protein receptor (SNARE) complex assembly at the endoplasmic reticulum in Saccharomyces cerevisiae. *J. Biol. Chem.* 286:25027–25038. https://doi.org/10.1074/jbc.M110.215657

Ding, Y., S. Zhang, L. Yang, H. Na, P. Zhang, H. Zhang, Y. Wang, Y. Chen, J. Yu, C. Huo, et al. 2013. Isolating lipid droplets from multiple species. *Nat. Protoc.* 8:43–51. https://doi.org/10.1038/nprot.2012.142

Farese, R.V. Jr., and T.C. Walther. 2009. Lipid droplets finally get a little R-E-S-P-E-C-T. *Cell.* 139:855–860. https://doi.org/10.1016/j.cell.2009.11.005

Fei, W., G. Shui, B. Gaeta, X. Du, L. Kuerschner, P. Li, A.J. Brown, M.R. Wenk, R.G. Parton, and H. Yang. 2008. Fld1p, a functional homologue of human seipin, regulates the size of lipid droplets in yeast. *J. Cell Biol.* 180:473–482. https://doi.org/10.1083/jcb.200711136

Fei, W., G. Shui, Y. Zhang, N. Krahmer, C. Ferguson, T.S. Kapterian, R.C. Lin, I.W. Dawes, A.J. Brown, P. Li, et al. 2011. A role for phosphatidic acid in the formation of "supersized" lipid droplets. *PLoS Genet.* 7:e1002201. https://doi.org/10.1371/journal.pgen.1002201

Fujimoto, Y., H. Itabe, T. Kinoshita, K.J. Homma, J. Onoduka, M. Mori, S. Yamaguchi, M. Makita, Y. Higashi, A. Yamashita, and T. Takano. 2007. Involvement of ACSL in local synthesis of neutral lipids in cytoplasmic lipid droplets in human hepatocyte HuH7. *J. Lipid Res.* 48:1280–1292. https://doi.org/10.1194/jlr.M700050-JLR200

Gerondopoulos, A., R.N. Bastos, S. Yoshimura, R. Anderson, S. Carpanini, I. Aligianis, M.T. Handley, and F.A. Barr. 2014. Rab18 and a Rab18 GEF complex are required for normal ER structure. *J. Cell Biol.* 205:707–720. https://doi.org/10.1083/jcb.201403026

Gillingham, A.K., R. Sinka, I.L. Torres, K.S. Lilley, and S. Munro. 2014. Toward a comprehensive map of the effectors of rab GTPases. *Dev. Cell.* 31:358–373. https://doi.org/10.1016/j.devcel.2014.10.007

Gong, J., Z. Sun, and P. Li. 2009. CIDE proteins and metabolic disorders. *Curr. Opin. Lipidol.* 20:121–126. https://doi.org/10.1097/MOL.0b013e328328d0bb

Gong, J., Z. Sun, L. Wu, W. Xu, N. Schieber, D. Xu, G. Shui, H. Yang, R.G. Parton, and P. Li. 2011. Fsp27 promotes lipid droplet growth by lipid exchange and transfer at lipid droplet contact sites. *J. Cell Biol.* 195:953–963. https://doi.org/10.1083/jcb.201104142

Greenberg, A.S., R.A. Coleman, F.B. Kraemer, J.L. McManaman, M.S. Obin, V. Puri, Q.W. Yan, H. Miyoshi, and D.G. Mashek. 2011. The role of lipid droplets in metabolic disease in rodents and humans. *J. Clin. Invest.* 121:2102–2110. https://doi.org/10.1172/JCI46069

Grippa, A., L. Buxó, G. Mora, C. Funaya, F.Z. Idrissi, F. Mancuso, R. Gomez, J. Muntanyà, E. Sabidó, and P. Carvalho. 2015. The seipin complex Fld1/Ldb16 stabilizes ER-lipid droplet contact sites. *J. Cell Biol.* 211:829–844. https://doi.org/10.1083/jcb.201502070

Gross, D.A., and D.L. Silver. 2014. Cytosolic lipid droplets: from mechanisms of fat storage to disease. *Crit. Rev. Biochem. Mol. Biol.* 49:304–326. https://doi.org/10.3109/10409238.2014.931337

Gross, D.A., C. Zhan, and D.L. Silver. 2011. Direct binding of triglyceride to fat storage-inducing transmembrane proteins 1 and 2 is important for lipid

droplet formation. *Proc. Natl. Acad. Sci. USA.* 108:19581–19586. https://doi.org/10.1073/pnas.1110817108

Grosshans, B.L., D. Ortiz, and P. Novick. 2006. Rabs and their effectors: achieving specificity in membrane traffic. *Proc. Natl. Acad. Sci. USA.* 103:11821–11827. https://doi.org/10.1073/pnas.0601617103

Han, S., D.D. Binns, Y.-F. Chang, and J.M. Goodman. 2015. Dissecting seipin function: the localized accumulation of phosphatidic acid at ER/LD junctions in the absence of seipin is suppressed by Sei1p(ΔNterm) only in combination with Ldb16p. *BMC Cell Biol.* 16:29. https://doi.org/10.1186/s12860-015-0075-3

Handley, M.T., and I.A. Aligianis. 2012. RAB3GAP1, RAB3GAP2 and RAB18: disease genes in Micro and Martsolf syndromes. *Biochem. Soc. Trans.* 40:1394–1397. https://doi.org/10.1042/BST20120169

Handley, M.T., D.J. Morris-Rosendahl, S. Brown, F. Macdonald, C. Hardy, D. Bem, S.M. Carpanini, G. Borck, L. Martorell, C. Izzi, et al. 2013. Mutation spectrum in RAB3GAP1, RAB3GAP2, and RAB18 and genotype-phenotype correlations in warburg micro syndrome and Martsolf syndrome. *Hum. Mutat.* 34:686–696. https://doi.org/10.1002/humu.22296

Hatsuzawa, K., H. Hirose, K. Tani, A. Yamamoto, R.H. Scheller, and M. Tagaya. 2000. Syntaxin 18, a SNAP receptor that functions in the endoplasmic reticulum, intermediate compartment, and cis-Golgi vesicle trafficking. *J. Biol. Chem.* 275:13713–13720. https://doi.org/10.1074/jbc.275.18.13713

Herker, E., C. Harris, C. Hernandez, A. Carpentier, K. Kaehlcke, A.R. Rosenberg, R.V. Farese Jr., and M. Ott. 2010. Efficient hepatitis C virus particle formation requires diacylglycerol acyltransferase-1. *Nat. Med.* 16:1295–1298. https://doi.org/10.1038/nm.2238

Hirose, H., K. Arasaki, N. Dohmae, K. Takio, K. Hatsuzawa, M. Nagahama, K. Tani, A. Yamamoto, M. Tohyama, and M. Tagaya. 2004. Implication of ZW10 in membrane trafficking between the endoplasmic reticulum and Golgi. *EMBO J.* 23:1267–1278. https://doi.org/10.1038/sj.emboj.7600135

Jacquier, N., V. Choudhary, M. Mari, A. Toulmay, F. Reggiori, and R. Schneiter. 2011. Lipid droplets are functionally connected to the endoplasmic reticulum in Saccharomyces cerevisiae. *J. Cell Sci.* 124:2424–2437. https://doi.org/10.1242/jcs.076836

Kamena, F., and A. Spang. 2004. Tip20p prohibits back-fusion of COPII vesicles with the endoplasmic reticulum. *Science.* 304:286–289. https://doi.org/10.1126/science.1095049

Kassan, A., A. Herms, A. Fernández-Vidal, M. Bosch, N.L. Schieber, B.J. Reddy, A. Fajardo, M. Gelabert-Baldrich, F. Tebar, C. Enrich, et al. 2013. Acyl-CoA synthetase 3 promotes lipid droplet biogenesis in ER microdomains. *J. Cell Biol.* 203:985–1001. https://doi.org/10.1083/jcb.201305142

Khandelia, H., L. Duelund, K.I. Pakkanen, and J.H. Ipsen. 2010. Triglyceride blisters in lipid bilayers: implications for lipid droplet biogenesis and the mobile lipid signal in cancer cell membranes. *PLoS One.* 5:e12811. https://doi.org/10.1371/journal.pone.0012811

Klemm, E.J., E. Spooner, and H.L. Ploegh. 2011. Dual role of ancient ubiquitous protein 1 (AUP1) in lipid droplet accumulation and endoplasmic reticulum (ER) protein quality control. *J. Biol. Chem.* 286:37602–37614. https://doi.org/10.1074/jbc.M111.284794

Krahmer, N., Y. Guo, F. Wilfling, M. Hilger, S. Lingrell, K. Heger, H.W. Newman, M. Schmidt-Supprian, D.E. Vance, M. Mann, et al. 2011. Phosphatidylcholine synthesis for lipid droplet expansion is mediated by localized activation of CTP:phosphocholine cytidylyltransferase. *Cell Metab.* 14:504–515. https://doi.org/10.1016/j.cmet.2011.07.013

Krahmer, N., R.V. Farese Jr., and T.C. Walther. 2013. Balancing the fat: lipid droplets and human disease. *EMBO Mol. Med.* 5:973–983. https://doi.org/10.1002/emmm.201100671

Kraynack, B.A., A. Chan, E. Rosenthal, M. Essid, B. Umansky, M.G. Waters, and H.D. Schmitt. 2005. Dsl1p, Tip20p, and the novel Dsl3(Sec39) protein are required for the stability of the Q/t-SNARE complex at the endoplasmic reticulum in yeast. *Mol. Biol. Cell.* 16:3963–3977. https://doi.org/10.1091/mbc.E05-01-0056

Kuerschner, L., C. Moessinger, and C. Thiele. 2008. Imaging of lipid biosynthesis: how a neutral lipid enters lipid droplets. *Traffic.* 9:338–352. https://doi.org/10.1111/j.1600-0854.2007.00689.x

Lam, S.S., J.D. Martell, K.J. Kamer, T.J. Deerinck, M.H. Ellisman, V.K. Mootha, and A.Y. Ting. 2015. Directed evolution of APEX2 for electron microscopy and proximity labeling. *Nat. Methods.* 12:51–54. https://doi.org/10.1038/nmeth.3179

Li, C., X. Luo, S. Zhao, G.K. Siu, Y. Liang, H.C. Chan, A. Satoh, and S.S. Yu. 2017. COPI-TRAPPII activates Rab18 and regulates its lipid droplet association. *EMBO J.* 36:441–457. https://doi.org/10.15252/embj.201694866

Li, Z., K. Thiel, P.J. Thul, M. Beller, R.P. Kühnlein, and M.A. Welte. 2012. Lipid droplets control the maternal histone supply of Drosophila embryos. *Curr. Biol.* 22:2104–2113. https://doi.org/10.1016/j.cub.2012.09.018

Liegel, R.P., M.T. Handley, A. Ronchetti, S. Brown, L. Langemeyer, A. Linford, B. Chang, D.J. Morris-Rosendahl, S. Carpanini, R. Posmyk, et al. 2013. Loss-of-function mutations in TBC1D20 cause cataracts and male infertility in blind sterile mice and Warburg micro syndrome in humans. *Am. J. Hum. Genet.* 93:1001–1014. https://doi.org/10.1016/j.ajhg.2013.10.011

Liu, L., K. Zhang, H. Sandoval, S. Yamamoto, M. Jaiswal, E. Sanz, Z. Li, J. Hui, B.H. Graham, A. Quintana, and H.J. Bellen. 2015. Glial lipid droplets and ROS induced by mitochondrial defects promote neurodegeneration. *Cell.* 160:177–190. https://doi.org/10.1016/j.cell.2014.12.019

Magré, J., M. Delépine, E. Khallouf, T. Gedde-Dahl Jr., L. Van Maldergem, E. Sobel, J. Papp, M. Meier, A. Mégarbané, A. Bachy, et al. BSCL Working Group. 2001. Identification of the gene altered in Berardinelli-Seip congenital lipodystrophy on chromosome 11q13. *Nat. Genet.* 28:365–370. https://doi.org/10.1038/ng585

Martin, S., and R.G. Parton. 2006. Lipid droplets: a unified view of a dynamic organelle. *Nat. Rev. Mol. Cell Biol.* 7:373–378. https://doi.org/10.1038/nrm1912

Martin, S., and R.G. Parton. 2008. Characterization of Rab18, a lipid droplet-associated small GTPase. *Methods Enzymol.* 438:109–129. https://doi.org/10.1016/S0076-6879(07)38008-7

Martin, S., K. Driessen, S.J. Nixon, M. Zerial, and R.G. Parton. 2005. Regulated localization of Rab18 to lipid droplets: effects of lipolytic stimulation and inhibition of lipid droplet catabolism. *J. Biol. Chem.* 280:42325–42335. https://doi.org/10.1074/jbc.M506651200

Meiringer, C.T., R. Rethmeier, K. Auffarth, J. Wilson, A. Perz, C. Barlowe, H.D. Schmitt, and C. Ungermann. 2011. The Dsl1 protein tethering complex is a resident endoplasmic reticulum complex, which interacts with five soluble NSF (N-ethylmaleimide-sensitive factor) attachment protein receptors (SNAREs): implications for fusion and fusion regulation. *J. Biol. Chem.* 286:25039–25046. https://doi.org/10.1074/jbc.M110.215327

Murphy, D.J., and J. Vance. 1999. Mechanisms of lipid-body formation. *Trends Biochem. Sci.* 24:109–115. https://doi.org/10.1016/S0968-0004(98)01349-8

Nakajima, K., H. Hirose, M. Taniguchi, H. Kurashina, K. Arasaki, M. Nagahama, K. Tani, A. Yamamoto, and M. Tagaya. 2004. Involvement of BNIP1 in apoptosis and endoplasmic reticulum membrane fusion. *EMBO J.* 23:3216–3226. https://doi.org/10.1038/sj.emboj.7600333

Nian, Z., Z. Sun, L. Yu, S.Y. Toh, J. Sang, and P. Li. 2010. Fat-specific protein 27 undergoes ubiquitin-dependent degradation regulated by triacylglycerol synthesis and lipid droplet formation. *J. Biol. Chem.* 285:9604–9615. https://doi.org/10.1074/jbc.M109.043786

Ohsaki, Y., J. Cheng, M. Suzuki, A. Fujita, and T. Fujimoto. 2008. Lipid droplets are arrested in the ER membrane by tight binding of lipidated apolipoprotein B-100. *J. Cell Sci.* 121:2415–2422. https://doi.org/10.1242/jcs.025452

Ota, T., C. Gayet, and H.N. Ginsberg. 2008. Inhibition of apolipoprotein B100 secretion by lipid-induced hepatic endoplasmic reticulum stress in rodents. *J. Clin. Invest.* 118:316–332. https://doi.org/10.1172/JCI32752

Ozeki, S., J. Cheng, K. Tauchi-Sato, N. Hatano, H. Taniguchi, and T. Fujimoto. 2005. Rab18 localizes to lipid droplets and induces their close apposition to the endoplasmic reticulum-derived membrane. *J. Cell Sci.* 118:2601–2611. https://doi.org/10.1242/jcs.02401

Pagac, M., D.E. Cooper, Y. Qi, I.E. Lukmantara, H.Y. Mak, Z. Wu, Y. Tian, Z. Liu, M. Lei, X. Du, et al. 2016. SEIPIN Regulates Lipid Droplet Expansion and Adipocyte Development by Modulating the Activity of Glycerol-3-phosphate Acyltransferase. *Cell Reports.* 17:1546–1559. https://doi.org/10.1016/j.celrep.2016.10.037

Payne, V.A., N. Grimsey, A. Tuthill, S. Virtue, S.L. Gray, E. Dalla Nora, R.K. Semple, S. O'Rahilly, and J.J. Rochford. 2008. The human lipodystrophy gene BSCL2/seipin may be essential for normal adipocyte differentiation. *Diabetes.* 57:2055–2060. https://doi.org/10.2337/db08-0184

Pol, A., S.P. Gross, and R.G. Parton. 2014. Review: Biogenesis of the multifunctional lipid droplet: Lipids, proteins, and sites. *J. Cell Biol.* 204:635–646. https://doi.org/10.1083/jcb.201311051

Pulido, M.R., A. Diaz-Ruiz, Y. Jiménez-Gómez, S. Garcia-Navarro, F. Gracia-Navarro, F. Tinahones, J. López-Miranda, G. Frühbeck, R. Vázquez-Martínez, and M.M. Malagón. 2011. Rab18 dynamics in adipocytes in relation to lipogenesis, lipolysis and obesity. *PLoS One.* 6:e22931. https://doi.org/10.1371/journal.pone.0022931

Ran, F.A., P.D. Hsu, J. Wright, V. Agarwala, D.A. Scott, and F. Zhang. 2013. Genome engineering using the CRISPR-Cas9 system. *Nat. Protoc.* 8:2281–2308. https://doi.org/10.1038/nprot.2013.143

Ren, Y., C.K. Yip, A. Tripathi, D. Huie, P.D. Jeffrey, T. Walz, and F.M. Hughson. 2009. A structure-based mechanism for vesicle capture by the multisubunit tethering complex Dsl1. *Cell.* 139:1119–1129. https://doi.org/10.1016/j.cell.2009.11.002

Salloum, S., H. Wang, C. Ferguson, R.G. Parton, and A.W. Tai. 2013. Rab18 binds to hepatitis C virus NS5A and promotes interaction between sites of viral replication and lipid droplets. *PLoS Pathog.* 9:e1003513. https://doi.org/10.1371/journal.ppat.1003513

Salo, V.T., I. Belevich, S. Li, L. Karhinen, H. Vihinen, C. Vigouroux, J. Magré, C. Thiele, M. Hölttä-Vuori, E. Jokitalo, and E. Ikonen. 2016. Seipin regulates ER-lipid droplet contacts and cargo delivery. *EMBO J.* 35:2699–2716. https://doi.org/10.15252/embj.201695170

Shen, W.J., S. Azhar, and F.B. Kraemer. 2016. Lipid droplets and steroidogenic cells. *Exp. Cell Res.* 340:209–214. https://doi.org/10.1016/j.yexcr.2015.11.024

Stenmark, H. 2009. Rab GTPases as coordinators of vesicle traffic. *Nat. Rev. Mol. Cell Biol.* 10:513–525. https://doi.org/10.1038/nrm2728

Sun, Z., J. Gong, H. Wu, W. Xu, L. Wu, D. Xu, J. Gao, J.W. Wu, H. Yang, M. Yang, and P. Li. 2013a. Perilipin1 promotes unilocular lipid droplet formation through the activation of Fsp27 in adipocytes. *Nat. Commun.* 4:1594. https://doi.org/10.1038/ncomms2581

Sun, Z., J. Gong, L. Wu, and P. Li. 2013b. Imaging lipid droplet fusion and growth. *Methods Cell Biol.* 116:253–268. https://doi.org/10.1016/B978-0-12-408051-5.00013-9

Suzuki, M., Y. Shinohara, Y. Ohsaki, and T. Fujimoto. 2011. Lipid droplets: size matters. *J. Electron Microsc. (Tokyo).* 60(Suppl. 1):S101–S116. https://doi.org/10.1093/jmicro/dfr016

Suzuki, M., T. Otsuka, Y. Ohsaki, J. Cheng, T. Taniguchi, H. Hashimoto, H. Taniguchi, and T. Fujimoto. 2012. Derlin-1 and UBXD8 are engaged in dislocation and degradation of lipidated ApoB-100 at lipid droplets. *Mol. Biol. Cell.* 23:800–810. https://doi.org/10.1091/mbc.E11-11-0950

Szymanski, K.M., D. Binns, R. Bartz, N.V. Grishin, W.P. Li, A.K. Agarwal, A. Garg, R.G. Anderson, and J.M. Goodman. 2007. The lipodystrophy protein seipin is found at endoplasmic reticulum lipid droplet junctions and is important for droplet morphology. *Proc. Natl. Acad. Sci. USA.* 104:20890–20895. https://doi.org/10.1073/pnas.0704154104

Tagaya, M., K. Arasaki, H. Inoue, and H. Kimura. 2014. Moonlighting functions of the NRZ (mammalian Dsl1) complex. *Front. Cell Dev. Biol.* 2:25. https://doi.org/10.3389/fcell.2014.00025

Thiam, A.R., R.V. Farese Jr., and T.C. Walther. 2013. The biophysics and cell biology of lipid droplets. *Nat. Rev. Mol. Cell Biol.* 14:775–786. https://doi.org/10.1038/nrm3699

Tripathi, A., Y. Ren, P.D. Jeffrey, and F.M. Hughson. 2009. Structural characterization of Tip20p and Dsl1p, subunits of the Dsl1p vesicle tethering complex. *Nat. Struct. Mol. Biol.* 16:114–123. https://doi.org/10.1038/nsmb.1548

Walther, T.C., and R.V. Farese Jr. 2012. Lipid droplets and cellular lipid metabolism. *Annu. Rev. Biochem.* 81:687–714. https://doi.org/10.1146/annurev-biochem-061009-102430

Wang, H., M. Becuwe, B.E. Housden, C. Chitraju, A.J. Porras, M.M. Graham, X.N. Liu, A.R. Thiam, D.B. Savage, A.K. Agarwal, et al. 2016. Seipin is required for converting nascent to mature lipid droplets. *eLife.* 5:5. https://doi.org/10.7554/eLife.16582

Wang, W., N. Lv, S. Zhang, G. Shui, H. Qian, J. Zhang, Y. Chen, J. Ye, Y. Xie, Y. Shen, et al. 2012. Cidea is an essential transcriptional coactivator regulating mammary gland secretion of milk lipids. *Nat. Med.* 18:235–243. https://doi.org/10.1038/nm.2614

Wilfling, F., H. Wang, J.T. Haas, N. Krahmer, T.J. Gould, A. Uchida, J.X. Cheng, M. Graham, R. Christiano, F. Fröhlich, et al. 2013. Triacylglycerol synthesis enzymes mediate lipid droplet growth by relocalizing from the ER to lipid droplets. *Dev. Cell.* 24:384–399. https://doi.org/10.1016/j.devcel.2013.01.013

Wilfling, F., J.T. Haas, T.C. Walther, and R.V. Farese Jr. 2014. Lipid droplet biogenesis. *Curr. Opin. Cell Biol.* 29:39–45. https://doi.org/10.1016/j.ceb.2014.03.008

Wu, L., D. Xu, L. Zhou, B. Xie, L. Yu, H. Yang, L. Huang, J. Ye, H. Deng, Y.A. Yuan, et al. 2014a. Rab8a-AS160-MSS4 regulatory circuit controls lipid droplet fusion and growth. *Dev. Cell.* 30:378–393. https://doi.org/10.1016/j.devcel.2014.07.005

Wu, L., L. Zhou, C. Chen, J. Gong, L. Xu, J. Ye, D. Li, and P. Li. 2014b. Cidea controls lipid droplet fusion and lipid storage in brown and white adipose tissue. *Sci. China Life Sci.* 57:107–116. https://doi.org/10.1007/s11427-013-4585-y

Xu, L., L. Zhou, and P. Li. 2012a. CIDE proteins and lipid metabolism. *Arterioscler. Thromb. Vasc. Biol.* 32:1094–1098. https://doi.org/10.1161/ATVBAHA.111.241489

Xu, N., S.O. Zhang, R.A. Cole, S.A. McKinney, F. Guo, J.T. Haas, S. Bobba, R.V. Farese Jr., and H.Y. Mak. 2012b. The FATP1-DGAT2 complex facilitates lipid droplet expansion at the ER-lipid droplet interface. *J. Cell Biol.* 198:895–911. https://doi.org/10.1083/jcb.201201139

Xu, W., L. Wu, M. Yu, F.J. Chen, M. Arshad, X. Xia, H. Ren, J. Yu, L. Xu, D. Xu, et al. 2016. Differential Roles of Cell Death-inducing DNA Fragmentation Factor-α-like Effector (CIDE) Proteins in Promoting Lipid Droplet Fusion and Growth in Subpopulations of Hepatocytes. *J. Biol. Chem.* 291:4282–4293. https://doi.org/10.1074/jbc.M115.701094

Yamaguchi, T., N. Fujikawa, S. Nimura, Y. Tokuoka, S. Tsuda, T. Aiuchi, R. Kato, T. Obama, and H. Itabe. 2015. Characterization of lipid droplets in steroidogenic MLTC-1 Leydig cells: Protein profiles and the morphological change induced by hormone stimulation. *Biochim. Biophys. Acta.* 1851:1285–1295. https://doi.org/10.1016/j.bbalip.2015.06.007

Yang, H., A. Galea, V. Sytnyk, and M. Crossley. 2012. Controlling the size of lipid droplets: lipid and protein factors. *Curr. Opin. Cell Biol.* 24:509–516. https://doi.org/10.1016/j.ceb.2012.05.012

Zanghellini, J., F. Wodlei, and H.H. von Grünberg. 2010. Phospholipid demixing and the birth of a lipid droplet. *J. Theor. Biol.* 264:952–961. https://doi.org/10.1016/j.jtbi.2010.02.025

Zerial, M., and H. McBride. 2001. Rab proteins as membrane organizers. *Nat. Rev. Mol. Cell Biol.* 2:107–117. https://doi.org/10.1038/35052055

Zhang, S., G. Shui, G. Wang, C. Wang, S. Sun, C.C. Zouboulis, R. Xiao, J. Ye, W. Li, and P. Li. 2014. Cidea control of lipid storage and secretion in mouse and human sebaceous glands. *Mol. Cell. Biol.* 34:1827–1838. https://doi.org/10.1128/MCB.01723-13

Zhou, L., L. Xu, J. Ye, D. Li, W. Wang, X. Li, L. Wu, H. Wang, F. Guan, and P. Li. 2012. Cidea promotes hepatic steatosis by sensing dietary fatty acids. *Hepatology.* 56:95–107. https://doi.org/10.1002/hep.25611